

Research Paper

Influence of eccentricity on the thermomechanical performance of a bayonet tube of a central solar receiver

Rafael Pérez-Álvarez^{*}, Carolina Marugán-Cruz, Domingo Santana, Antonio Acosta-Iborra

Department of Thermal and Fluids Engineering, Carlos III University of Madrid, Avda. de la Universidad 30, 28911 Leganés, Madrid, Spain

ARTICLE INFO

Keywords:

Solar tower plant
Eccentric bayonet tubes
Non-uniform heating
Convection heat transfer
Thermal stresses
Numerical simulation

ABSTRACT

This work numerically evaluates the thermal and mechanical behaviors of eccentric bayonet tubes to be used in external central receivers of solar power tower plants. A bayonet tube is composed of two tubes, one inside the other, creating circular and annular sections, through which the molten salt of the receiver sequentially flows. Eccentricity in the annular section is achieved by displacing the axis of the interior tube with regard to the exterior one. For comparative purposes, two examples of conventional tubes (single tubes with circular cross-sections with diameters of 25 mm and 50 mm) are also investigated in this work to compare their performances with those of bayonet tubes. The results obtained with the eccentric configurations show an enhancement of the heat transfer to the molten salt and a reduction of the tube wall overheating compared with the concentric bayonet tubes and the largest simple tube. For conditions representative of the normal operation of a solar power tower, eccentric bayonet tubes could reduce the pressure drop by 30.8% and increase the convective heat transfer achieved in a concentric configuration of the bayonet tube by 26.1%. Nevertheless, this pressure drop was considerably higher than those obtained in the smallest and largest simple tubes, which were 1.28 bar and 0.13 bar, respectively. To investigate whether the enhancement of the convection heat transfer experienced by bayonet tubes compensates for their higher pressure drop or not, a *Performance Evaluation Criterion* (PEC) was proposed and used to compare the global performance of bayonet tubes with that of conventional tubes. The bayonet tubes with eccentricity 0.45 obtained the largest PEC, which was up to 13% higher than reference conventional tubes. Enhancement of the tube wall refrigeration produced when increasing the eccentricity is reflected in the maximum tube temperature and thermal stresses, which are found to diminish by approximately 8.8% with the highest eccentricity. In addition, the largest eccentric bayonet tube layout obtains the smallest peak temperatures compared to conventional tubes. The lower inertial moment of the smallest conventional tube indicates that its thermal stress is 2.1% lower than the stress obtained in the most eccentric layout analyzed in this work. Nevertheless, the time to rupture associated with creep damage of the eccentric bayonet tube is 1.04 times higher than that obtained in the smallest simple tube, demonstrating that bayonet tubes could be a potential alternative to the current tubes of external tubular receivers.

1. Introduction

The receiver tubes of solar power tower (SPT) plants are subjected to high thermal gradients generated by nonuniform solar radiation, which is concentrated by the heliostat field on the receiver surface. According to [1], these thermal gradients combined with molten salt corrosion and solar flux transients lead to high thermal stresses, which could derive in severe creep and fatigue damages on the receiver, rupturing its absorber tubes and limiting the operation of the plant. In the aforementioned work, the authors discussed the relevance of film temperature since it is responsible for salt decomposition and tube corrosion. They reported that the smallest tube diameters yielded low film temperatures, but with the highest pressure drops. Thus, to

optimize the investment and operational cost of the receiver, they concluded that a compromise between film temperature and pressure drop is needed in the receiver design. Chen et al. [2] emphasized the importance of considering creep damage in the design process of receiver tubes. Du et al. [3] calculated the thermal stress and fatigue fracture of a representative tube of an external tubular receiver. In addition, the authors provided the minimum heat flux when damage occurs and the critical crack length, computed through the *Crack Tip Opening Displacement* (CTOD) method. In the literature, different options regarding how to increase the lifespans of the receiver tubes have been considered. One of these options is the enhancement of the tube wall refrigeration, which leads to a reduction in the thermal gradients of the receiver. Thus, a receiver whose layout enhances convection

^{*} Corresponding author.

E-mail address: rafperez@ing.uc3m.es (R. Pérez-Álvarez).

Nomenclature**Latin symbols**

c_p	Material specific heat ($\text{J kg}^{-1} \text{K}^{-1}$)
d	Diameter of the interior tube of bayonet tube (m)
D	Diameter of the exterior tube of bayonet tube/Diameter of simple tube (m)
D_h	Hydraulic diameter of the annular cross-section (m)
e	Axes tubes separation (m)
f	Friction factor
H_{CAP}	Bayonet cap height (m)
k	Material thermal conductivity ($\text{W m}^{-1} \text{K}^{-1}$)
k_{aim}	Aiming strategy
L	Tube length (m)
\dot{m}_b	Mass flow (kg s^{-1})
Nu	Nusselt number
Pr	Prandtl number
q''	Heat flux (W m^{-2})
r_c	Radial coordinate (m)
\bar{r}_c	Normalized radial coordinate
\vec{r}	vector of positions (m)
r	Radii of the interior tube (m)
R	Radii of the exterior tube (m)
Re	Reynolds number
R''_{foul}	Fouling resistance ($\text{K m}^2 \text{W}^{-1}$)
T	Temperature (K)
\bar{T}	Bulk temperature (K)
t_R	Time to rupture associated with creep damage (m)
v	Velocity (m s^{-1})
z	Axial coordinate (m)

Greek symbols

ΔS	Cell size (m)
ΔP	Pressure drop (Pa)
ξ	Eccentricity
μ	Material viscosity (Pa s)
ρ	Material density (kg m^{-3})
σ	Stress (MPa)
σ_θ	Circumferential stress (MPa)
σ_r	Radial stress (MPa)
σ_z	Axial stress (MPa)
θ	Circumferential coordinate ($^\circ$)
$\tau_{r,\theta}$	Shear stress (MPa)

Subscripts

abs	Absorbed
an	Annular
cap	Cap
$circ$	Circular
$creep$	Creep damage
e	Exterior surface
eff	Effective stress
i	Inner surface

IT	Interior tube
max	Maximum
OT	Exterior tube
$salt$	Salt
VM	von Mises

Abbreviations

DNI	Direct Normal Irradiation
DNS	Direct Numerical Simulation
CFD	Computational Fluid Dynamics
HTF	Heat Transfer Fluid
GPS	Generalized Plane Strain
LES	Large Eddy Simulations
$RANS$	Reynolds Average Navier–Stokes
SPT	Solar Power Tower
SST	Shear-Stress Transport

to improve the receiver reliability [4–8], while other authors devoted their investigation to alternative heat transfer fluids (HTF) [9–12]. The above-cited works were developed for steady-state conditions, but the transient states have been also considered in the literature, [13–16]. Rodríguez-Sánchez et al. [17] proposed an external receiver composed of bayonet tubes instead of simple tubes of circular cross-section. A bayonet tube comprises two tubes, one inside the other, creating a circular section and an annular section. The bayonet tube can improve the heat transfer of the molten salt due to the rise in the molten salt velocity in the vicinity of the zone with the most thermal demand. Furthermore, local overheating of the molten salt is avoided since a fraction of the heat absorbed by the outer tube is exchanged between the flow of molten salt in the annular section and the molten salt flowing in the circular section. When the axes of the exterior and interior tubes of the bayonet tube are not concentric, viz. an eccentric bayonet tube, the resulting asymmetry of the flow can be used to increase the convection heat transfer coefficient in the angular direction where the solar irradiation is at the maximum level, which opens the possibility of further reducing the temperature gradients of the bayonet tubes while maintaining the pressure drop [18]. Therefore, bayonet tubes offer extra degrees of freedom compared with simple tubes, a fact that can be used to optimize the thermomechanical behavior of the receiver. For this reason, it is worth considering the use of bayonet tubes in SPT receiver applications. There are also some related works of asymmetric ducts, but for parabolic trough collectors and not in bayonet configuration. Wang et al. [19] investigated the use of an eccentric annular gap, instead of a circular one, between the absorber tube and the glass envelope of a parabolic trough collector. The authors analyzed through a numerical model the effect of the incident irradiation angle and the eccentricity on the heat loss through the annulus with enclosed air or vacuum. They concluded that asymmetric characteristics had a significant influence on local heat transfer processes. In addition, Wang et al. [20] studied the effect of inserting metal foams asymmetrically plated in the receiver tube of a parabolic trough collector. They found that the heat transfer was enhanced and, depending on the size and the location of the metal foam in the tube, an optimum thermal or thermohydraulic performance was obtained. Chang et al. [21] analyzed the flow and convective heat transfer characteristics in the receiver tube of parabolic trough collectors with a circular rod insert in the tube. Their results showed that both the concentric and the eccentric rod configurations were able to significantly enhance the heat transfer performance for optimum rod parameters. However, hydrodynamic and thermal characterizations of eccentric bayonet tubes when used as absorber tubes in SPT plants have not been presented in the literature.

heat transfer may imply a lengthening of the receiver lifespan and could contribute to the maturation of SPT technology. Several authors have tried to optimize the receiver geometry or develop new designs

The study of the fluid flow and heat transfer in bayonet tubes is essential to understand and optimize them, especially the flow in the annular cross-section, which is more complex than the flow in circular sections. Concerning annular ducts, the literature about this topic can be organized into the following two groups: experimental and analytical/numerical analyses of fluid flow and heat transfer in concentric and eccentric annuli. Some exhaustive experimental characterization of annular ducts has been carried out in recent decades. Wolffe [22] investigated the flow of turbulent air through an annular passage set in a pipe of a circular section in which a fixed cylindrical core was set. In this work, the authors measured the air velocity and obtained its velocity pattern. In addition, the velocity isolines were obtained for concentric and eccentric configurations. An experimental characterization of the friction factor was provided by Dodge [23] for large diameter-ratio annular ducts. Kays and Leung [24] experimentally characterized the heat transfer of a turbulent flow in a concentric tube with a constant heat rate. They provided an asymptotic solution based on velocity and eddy diffusivity profiles for a wide range of Reynolds (Re), Prandtl (Pr), and radii ratios. Jonsson and Sparrow [25] characterized the features of the turbulent flow field and pressure drop for an eccentric annular duct. In an experiment, they varied the tube eccentricity from a concentric configuration to the maximum eccentricity where the walls of the exterior and interior tubes were in contact. They noticed a reduction in the friction drop when the eccentricity rose. In addition, they observed that the hydrodynamic development lengths increase with eccentricity. Kacker [26] studied the turbulent flow in a circular pipe that contained one or two rods. They checked the validity of the universal law of the wall close to the rod wall through mean velocity measurements. In addition, they reported the existence of secondary flows, whose magnitudes were approximately 1% of the mean velocity. Nouri et al. [27] measured the flow velocity components and their shear stresses for Newtonian and non-Newtonian fluids flowing inside concentric and eccentric annular ducts. Choueiri and Tavoularis [28] experimentally analyzed how the gap instability started in eccentric annular channels and how a vortex street was generated. The authors analyzed three different flow conditions, as follows: laminar, transition, and turbulent. This work was completed in another work by Choueiri and Tavoularis [29] through additional measurements to discuss the effects of the eccentricity, Reynolds number, inlet conditions, and radius ratio on the annular section instability and vortex streets. Serrano et al. [30] determined the convection heat transfer coefficient for different turbulent air flow rates in an eccentric annular duct and found that the magnitude of the convective heat transfer coefficient in an eccentric annular section depends on the angular position.

In addition to experimental works, there are a large number of analytical and numerical analyses in the literature devoted to annular ducts. Deissler and Taylor [31] characterized the heat transfer and the turbulent flow for an eccentric annular section through an analytical model, which assumed that the velocity profile of the fluid inside circular tubes could be applied for the annular passage along the normal direction to the bounding walls. Usui and Tsuruta [32] obtained the velocity distribution and the friction factor through a model based on the Kirchhoff transformation to analyze the turbulent flow for an eccentric passage. The authors compared their results with experimental measurements available in the literature and discussed the accuracy of their model, which was not able to accurately predict the secondary motion of the flow. They found that the shear stress for turbulent eccentric annular flow was similar to that obtained for a laminar flow. Other authors approached this problem through *direct numerical simulations* (DNSs). Ninokata et al. [33] solved the turbulent flow of an eccentric annulus channel with a DNS algorithm and used the finite difference method to analyze the local laminarization of the flow near the narrow gap region. Nikitin [34] solved the Navier–Stokes equations in curvilinear orthogonal coordinates through the use of a numerical algorithm. This method was used to obtain the mean

velocity, secondary motion, and turbulence intensity of a turbulent flow in an eccentric annular duct for $Re = 4000$. In addition, two different flow regimens were reported. Nikitin et al. [35] analyzed the turbulent heat transfer of an eccentric annular tube through a DNS. The authors provided the temperature, velocity, and Reynolds stress tensor and applied their turbulence modeling for flows with partial turbulent regimes. Merzari and Ninokata [36] discussed the anisotropy in the flow associated with different Reynolds numbers and eccentricities of the annular section through a numerical methodology based on *large eddy simulations* (LESs) with a fractional step algorithm and boundary fitted coordinates. They analyzed and discussed the behavior of the secondary flow for different Reynolds numbers and eccentricities.

In light of the above literature review, the option of substituting conventional tubes (i.e. circular cross-section tubes) with bayonet tubes in external tubular receivers of SPT plants has not been analyzed in detail. Although these works thoroughly characterized the turbulent flow in annular ducts, none of them analyzed the situation in which the walls of eccentric annular ducts were under nonuniform heating conditions and attempted to determine how this affects the temperature and stress distribution of the tube walls. This information would be relevant to assess the application of bayonet tubes to SPT receivers. Therefore, this work aims to investigate the effect of eccentricity on the thermomechanical performance of bayonet tubes. The nature of the bayonet tube behavior will be described via detailed numerical simulations to characterize variables such as velocity, temperature, convective heat transfer, pressure drop, and equivalent von Mises stress. In addition, to discuss the advantages and disadvantages of the potential use of bayonet tubes in SPT receivers, this work presents a comparison of the thermomechanical behavior of bayonet tubes and simple circular cross-section tubes. The conditions analyzed here are representative of the usual operation of an SPT receiver, where the tube heating is highly nonuniform.

2. System description

The thermal and hydrodynamic characterizations of both bayonet and simple tubes in this work were performed through a series of *computational fluid dynamics* (CFD) simulations. Eccentric and concentric layouts of bayonet tubes were studied to quantify the impact of eccentricity on the bayonet tube's performance. To provide a comparative framework, the bayonet tube results were compared with those of simple tubes. In the bayonet tube configuration analyzed here, named the inner bayonet configuration, the *heat transfer fluid* (HTF) to be heated is first pumped through the interior tube and then flows in the opposite direction through the annular section, which is the gap between the exterior and interior tubes, as shown Fig. 1(a). The bayonet tube performance under this configuration allows, for the same operating conditions, a lower pressure drop and wall temperature to be achieved compared to an outer bayonet configuration with an inverted flow direction (viz. molten salt enters through the annular passage), [37]. On its outer surface, the receiver tube is exposed to a nonuniform heat flux, q'' , which depends on the axial (z) and circumferential positions (θ), as shown Fig. 1. As mentioned before, the concentrated solar radiation absorbed by the exterior tube is then transferred to the flow in the annular section. A fraction of this heat is transferred through the interior tube walls to the flow inside this tube. As will be shown later, thanks to this layout, the bayonet tube can allow a reduction of the overheating that appears on the face where the solar radiation is at the maximum level, $\theta = 0^\circ$. The bayonet tube is geometrically defined by the outer and inner diameters of the exterior tube, D_e and D_i , respectively, and the outer and inner diameters of the interior tube, d_e and d_i , respectively, the length of the tube, L , and the eccentricity, ξ . In this work, for simplicity, the end cap of the bayonet tube was modeled as a flat cap, and its clearance height, H_{CAP} , was arbitrarily set equal to the annular hydraulic diameter ($H_{CAP} = D_h = D_i - d_e$) so that the flow has enough room to turn without excessively increasing

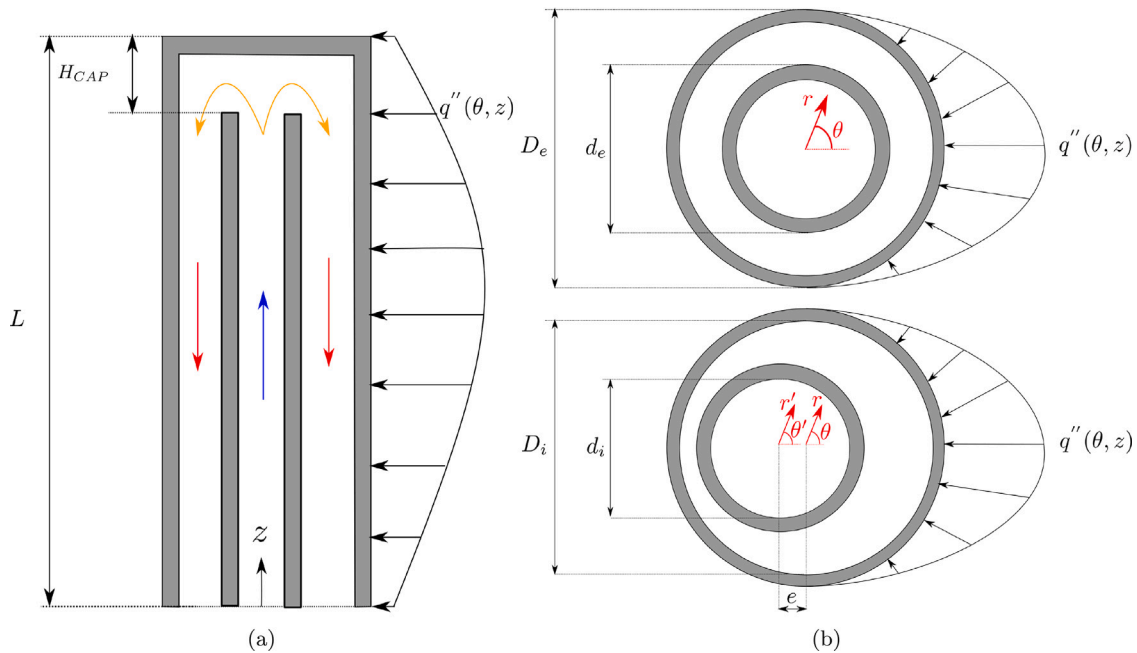


Fig. 1. Schematic representation of a bayonet tube with the description of the main geometric parameters and boundary conditions: (a) Section with an inner flow path configuration and flat end-cap, (b) Cross-section of the concentric (top) and eccentric (bottom) configurations.

its velocity modulus when passing from the circular tube to the annular gap. Eccentricity is defined as a function of the hydraulic diameter and the axis tube separation ($\xi = e/D_h$), where e is the distance between the axes of the exterior and interior tubes, as illustrated in Fig. 1(b). If $\xi = 0$, the bayonet tube is not eccentric but concentric. For simple tubes, i.e., circular cross-section tubes, only the following three variables are needed to define them geometrically: the length (L) and the outer and inner tube diameters (D_e and D_i , respectively).

In this work, the receiver of a Gemasolar SPT with both bayonet and simple tubes was analyzed. The Gemasolar receiver is configured as an external tubular receiver formed by panels of tubes, which create a 360° cylinder. The actual Gemasolar receiver, which has a height of 10.5 m and a diameter of 8.5 m, is formed by 18 panels, and each panel is composed of 56 simple tubes. Each of these tubes has an outer diameter of 25 mm and a tube thickness of 1.2 mm. The receiver has two flow paths with north-east-south and north-west-south orientations, which is a typical configuration according to [38]. The outer surface of each absorber tube is coated with a black Pyromark to increase the absorptivity of the solar radiation. For simplicity, it will be assumed that the tubes have an effective length for heat absorption equal to the receiver height, $L = 10.5$ m. In the Gemasolar receiver adapted to bayonet tubes, as described previously, the outer diameter of the exterior tube is set to 50 mm. The tube thickness is set to 1.4 mm for both the interior and the exterior tubes. The dimensions of the interior tube are set to $d_e = 34.75$ mm and $d_i = 31.95$ mm to achieve the same cross-section in the annular gap between tubes (A_{an}) as in the circular cross-section of the interior tube (A_{circ}). In addition to the bayonet tube, for the sake of comparison, the following two types of simple tubes were considered in this work: (i) the simple tube of the actual Gemasolar receiver (with an outer diameter of 25 mm and tube thickness of 1.2 mm), and (ii) a simple tube similar in size to the outer tube of the bayonet tube (with an outer diameter of 50 mm and a tube thickness of 1.4 mm, respectively). The tubes of each panel are made of Haynes 230, whose properties were modeled as temperature-dependent apart from its density, whose variation with temperature is comparatively much smaller than in the other properties [39,40]. The HTF flowing inside the absorber tubes is nitrate molten salt commonly known as solar salt, i.e., 60% wt NaNO_3 and 40% wt KNO_3 , whose properties were obtained from [41]. The properties of the tube material

and the HTF are summarized in Table 1. The values of the absorptivity and emissivity coefficients of the Pyromark materials were obtained from Zavoico [41] and Slem and Wade [42], respectively. The tubes of each panel are individually supported at one extreme, which permits unrestricted upward/downward thermal expansion. According to Falcone [43], the receiver tubes are periodically guided over their length by clips that are welded to the rear side of the tube. This mechanical attachment was similar for both the bayonet and the simple receiver tubes. The heliostat field considered in this work was similar to that of the Gemasolar SPT plant [44]. The solar noon of the spring equinox was selected as the representative day for the analysis since it can represent the average collective performance over the day and over the year [45]. The map of incident radiation concentrated over the receiver surface was provided by *SPTFlux* software [46] for a *direct normal irradiation* (DNI) of 900 W/m^2 and an aiming strategy defined $k_{aim} = 3$. For a given panel, all tubes were considered to have a similar spatial distribution of incident radiation on their surface because there are only slight differences between the incident radiation on a tube and that on their neighboring tubes. Therefore, as the simulation of an entire receiver panel would have a high computational cost, only a single representative tube in a panel needs to be studied. Specifically, the first north panel was selected in this work as the studied panel since it is subjected to the highest radiation flux and the lowest inlet temperature of the nitrate salt.

3. Thermal characterization

3.1. Governing equations

The continuity, momentum, and energy equations were solved to describe the flow of molten salt using the *Reynolds Average Navier–Stokes* (RANS) equations, expressed in the steady-state formulation and without viscous dissipation heating [47]. The *shear-stress transport* (SST) $k - \omega$ model [48] was chosen to obtain the turbulent parameters and the closure of the momentum and energy RANS equations of the flows since this turbulence model combines the robust and accurate formulation of the $k - \omega$ model in the near-wall region with the free-stream independence of the $k - \epsilon$ model in the far field [47].

Table 1
Material properties.

Zone	Material	Density ρ (kg/m ³)	Specific heat C_p (J/kg K)	Thermal conductivity k (W/m K)	Viscosity μ (Pa s)
Tube	Haynes 230	8970.0	$308.8 + 0.247 \cdot T(K)$	$2.937 + 0.02 \cdot T(K)$	–
HTF	Nitrate salt	$2263.7 - 0.636 \cdot T(K)$	$1396 + 0.172 \cdot T(K)$	$0.391 + 0.00019 \cdot T(K)$	$0.0755148 - 0.0002776 \cdot T(K)$ $+ 3.489 \cdot 10^{-7} \cdot T(K)^2$ $- 1.474 \cdot 10^{-10} \cdot T(K)^3$

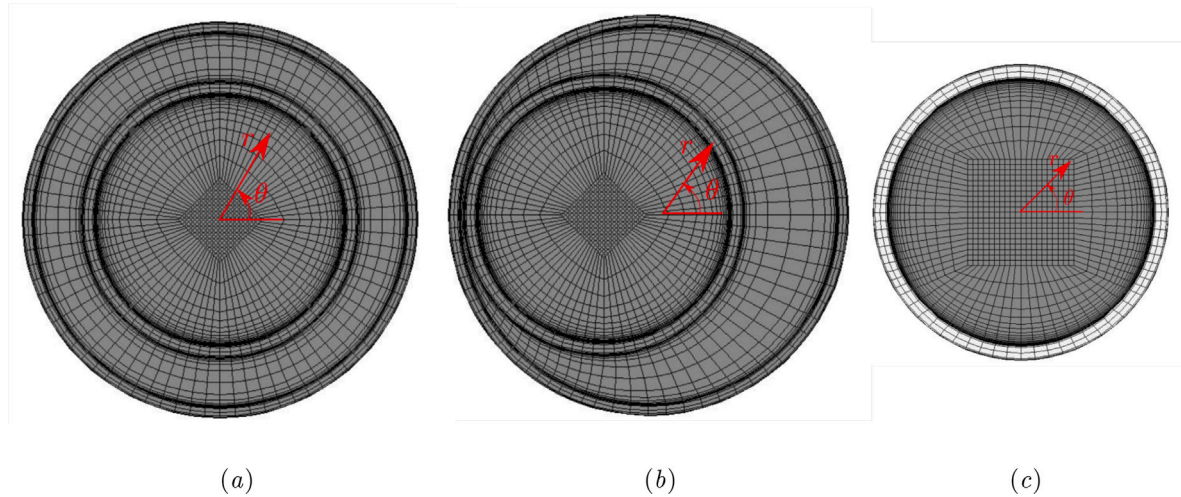


Fig. 2. Example of the cross-sections of the CFD numerical mesh selected in this work: (a) Concentric bayonet tube ($\xi = 0.00$), (b) Eccentric bayonet tube ($\xi = 0.45$), (c) Simple tube with the smallest diameter.

3.2. Numerical solution

The commercial software *ANSYS Fluent 2021R2* was used to solve the steady-state governing equations mentioned previously [47]. In the software, the equations are discretized with a pressure-based finite volume method [49] and are solved using the SIMPLE algorithm [50]. A second-order upwind method was used to discretize the convective and diffusive terms [51]. Solution iterations were stopped when the residuals of the equations reached a value below 10^{-6} . Moreover, the molten salt temperature at the tube's outlet was monitored to confirm the stabilization of the solution.

3.3. Computational mesh

The numerical model was solved using a structured 3D computational mesh with hexahedral cells in a 3D domain. The mesh included both the fluid in the tubes and the tube walls. The cell size was progressively reduced toward the tube walls to better reproduce and capture the molten salt boundary layer. An example of the cross-sections of the computational meshes generated for the bayonet tube in concentric and eccentric configurations is included in Figs. 2(a) and 2(b), respectively, while the mesh for a simple tube is shown in Fig. 2(c). The minimum cell size was set to guarantee that the $k - \omega$ turbulent model requirements, i.e., $y^+ \approx 1$ recommended by ANSYS were met [47]. Regarding the conditions of the SPT receivers, these requirements led to a cell size ranging from $5 \mu\text{m} \leq \Delta S \leq 15 \mu\text{m}$ at the contact surface between the molten salt and the tube walls. The mesh density inside the interior tube was not a determining factor since the velocity and temperature gradients were comparatively smaller in this region.

For each geometry employed in this work, a sensitivity analysis was performed to guarantee the independence of the results with the mesh. As an example, the results of the sensitivity analysis shown in this section were obtained for the smallest simple tube, i.e., the tube with an outer diameter of 25 mm and a thickness of 1.2 mm,

and for the concentric ($\xi = 0.00$) and eccentric ($\xi = 0.45$) bayonet tubes. For each sensitivity analysis, four meshes were developed. For the concentric and eccentric bayonet tubes, these meshes had $0.75 \cdot 10^5$, $1.25 \cdot 10^5$, $3.25 \cdot 10^5$ and $5.75 \cdot 10^5$ cells. The minimum cell size close to the tube walls was similar for all the meshes to guarantee the requirements of y^+ in the turbulent model. The maximum tube temperature and the bulk molten salt temperature at the tube outlet were selected to perform the sensitivity analysis due to the sensitivity of these variables to the mesh changes. The discrepancy in the results between the densest mesh, composed of $5.75 \cdot 10^5$ cells, and the mesh with $3.25 \cdot 10^5$ cells reached 1.18% and 0.16% for the maximum and bulk temperatures, respectively. Analogous results were obtained for the sensitivity analysis of the eccentric bayonet tube. Regarding the simple tube, four meshes with different numbers of cells ($0.76 \cdot 10^4$, $0.14 \cdot 10^5$, $0.98 \cdot 10^5$, and $2.12 \cdot 10^5$) were studied. These meshes have a smaller number of nodes than the bayonet tube model because the simple tube geometry is less complex. In the simple tube model, the variation in the results between the meshes with $2.12 \cdot 10^5$ cells and with $0.98 \cdot 10^5$ cells was 1.64% and 0.78% for the maximum and bulk temperatures, respectively. Therefore, meshes with $3.25 \cdot 10^5$ cells (bayonet tube) and $0.98 \cdot 10^5$ (simple tube) were selected for the rest of the analysis as a compromise between accuracy and computational cost. The meshes of the concentric and eccentric bayonet tubes comprised 80 elements in the circumferential direction, 10 elements in the tube thickness concentrated around the inner and outer surfaces of the tube, and 20 elements in the annular and circular narrows (Figs. 2(a) and 2(b)). The minimum orthogonal quality of the meshes was 0.652. The mesh of the simple tubes had 80 elements in the tube perimeter, 8 elements along the tube thickness, and 22 elements in the radial direction in the fluid domain. The minimum orthogonal quality of this mesh was 0.178 (Fig. 2(c)).

3.4. Boundary conditions and validation

As illustrated in Fig. 1, the heat flux absorbed by the tube is not uniform but depends on the angular and axial positions θ and z ,

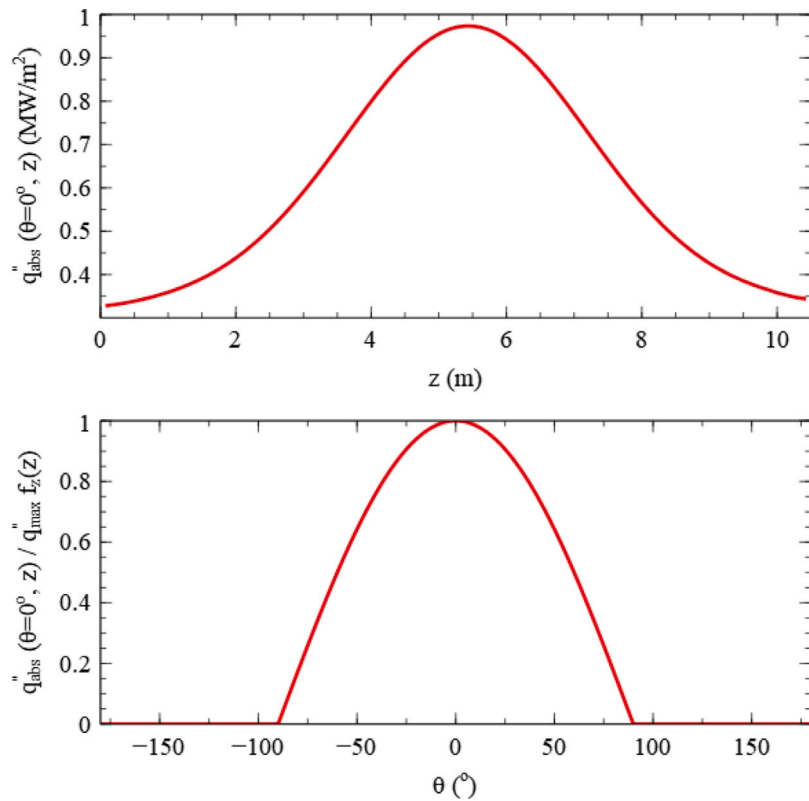


Fig. 3. Distribution of the net heat flux absorbed by the exterior surfaces of the tubes: (a) profile along the tube length at $\theta = 0^\circ$, (b) circumferential profile.

respectively. Due to the configurations of the external tubular receivers, the absorbed heat is at the maximum level on the tube side oriented to the field of heliostats, $\theta = 0^\circ$, while on the rear side of the tube, $|\theta| > 90^\circ$, only a residual heat flux is transferred from the reradiating surface and the surrounding tubes. To obtain computational resources in the 3D simulation, this residual heat flux can be neglected compared with the heat flux at the front side. Therefore, an adiabatic condition was imposed on the rear side.

Following a similar approach to several works in the literature, the circumferential distribution of the heat flux was modeled with a cosine function (see Eq. (1) and Fig. 3). This equation was applied as a boundary condition at the outer surface of the tube through a user-defined function (UDF).

$$q''_{abs}(\theta, z) = \begin{cases} q''_{max} \cdot \cos(\theta) \cdot f_z(z) & \text{if } |\theta| \leq 90^\circ \\ 0 & \text{if } |\theta| > 90^\circ \end{cases} \quad (1)$$

SPTflux software was employed to estimate the peak value of the incident heat flux and its axial variation along the tube length, q''_{max} and f_z , respectively. A representative value of the peak heat flux for a heliostat field similar to the Gemasolar SPT plant for the conditions studied in this work (i.e., spring equinox and an aiming strategy of a heliostat field equal to $k = 3$) was considered in this work ($q''_{max} = 979.55 \text{ kW/m}^2$). The axial heat flux variation was modeled through a fourth-grade Fourier series ($f_z(z) = a_0 + \sum_i a_i \cos(i \cdot z \cdot w) + b_i \sin(i \cdot z \cdot w)$) that depends on the axial position z , whose coefficient values are summarized in Table 2.

As mentioned above, the goal of this work is to unveil the main advantages or disadvantages of using bayonet tubes as absorber tubes in an external tubular receiver. Thus, to perform a fair comparison of bayonet and simple tubes, the same temperature increment of the molten salt inside the absorber tube was set for all the tubes analyzed in this work ($\Delta T = T_{out} - T_{in} = 37.6 \text{ }^\circ\text{C}$). The mass flow rate and temperature were specified to characterize the behavior of the molten

Table 2

Coefficients of fourth grade Fourier series used to describe the axial variation of the net heat flux.

i	a_i	b_i	w
0	0.5599	–	
1	–0.2676	0.1679	
2	0.0404	–0.0901	0.4742
3	0.0015	0.0188	
4	–0.001	–0.0012	

salt at the tube inlet. Both are imposed through a mass-flow inlet condition. The fluid temperature at the tube inlet was set to $290 \text{ }^\circ\text{C}$, while its mass flow was determined to reach a bulk fluid temperature of $565 \text{ }^\circ\text{C}$ at the receiver outlet. For the conditions studied in this work, this mass flow is $\dot{m} = 5.683 \text{ kg/s}$ for the bayonet tube and the largest simple tube, while it is 2.842 kg/s for the smallest simple tube, i.e., $D_e = 25 \text{ mm}$. At the tube outlet, pressure-outlet conditions were selected. At the wall surfaces in contact with the fluid, the nonslip condition was imposed for the molten salt velocity. As a result of the corrosion produced by the HTF during the receiver's previous operation, fouling inside the tubes needs to be considered. This fouling was included in the models through fouling resistance at the tube surfaces in contact with the molten salt, and its value ($R''_{fou} = 8.8 \cdot 10^{-5} \text{ Km}^2/\text{W}$) was obtained from [41]. Thus, these surfaces were thermally coupled with the fluid inside the tube through fouling resistance. For simplicity, the top and bottom cross-sections of the tube were considered adiabatic surfaces. It should be noted that the models proposed in this work were validated in two ways. One validation of the model was focused on the flow in a conventional tube and the other on the flow in an annular cross-section. In particular, the conventional tube model was validated through a comparison between the thermal results obtained in a numerical model and the results reported by Ying et al. [52]. In that work, the authors investigated the influence of gaussian-cosine heat flux on the thermal performance of the conventional circular tube

of a solar receiver with a molten salt-based nanofluid as HTF. The maximum temperature discrepancy between both models was 3.73%. The validation of the bayonet tube model was done for the flow in the annular cross-section with concentric configuration due to the lack of experimental measurements for eccentric annular ducts applicable to the Reynolds and Prandtl numbers of the molten salt flow here studied. To perform a fair comparison, we have developed additional simulations where the concentric bayonet tube was heated under axially- and circumferentially-uniform heat flux. The results of this simulation were compared with the general correlation of Gnielinski [53] and with the concentric annular duct correlation of Monrad and Pelton [54]. The comparison showed a good agreement between the CFD model and these correlations. For example, when the mean Reynolds and Prandtl numbers were $\overline{Re}_{an} = 25.67 \cdot 10^3$ and $\overline{Pr}_{an} = 10.1$, the maximum discrepancies between the Nusselt number obtained with the different correlations and the CFD model was below to 1.83%.

4. Mechanical characterization

For the mechanical characterization of the receiver tubes, the temperature field obtained from the CFD simulations was used in combination with the analytical methodology presented by Laporte-Azcué et al. [55]. This methodology was developed to calculate the elastic thermal stresses of circular tubes as a function of the nonaxisymmetrical temperature distribution. The use of this methodology was validated for steady and transient simulations in [55] and [13] respectively. To prevent excessive bowing, the receiver tubes are guided periodically over their length by mechanical attachments spaced at increments along the entire heights of the tubes. Based on the literature, *generalized plane strain* (GPS) conditions were considered in the elastic-stress analysis since these conditions are a good approach when the tube displacement is restricted by clips [56,57]. Note that GPS conditions allow the free axial expansion of the tubes and prevent excessive bowing generated by the temperature. The stress field of the bayonet tube under GPS conditions is composed of the superposition of the axial (σ_z), radial (σ_r), circumferential (σ_θ) and shear ($\tau_{r,\theta}$) stress components. Then, the absorber tube has a multiaxial stress state. As mentioned before, the simple tube and the exterior tube of the bayonet tube each have a mechanical attachment similar to that of conventional receiver tubes. In a real scenario, the interior tube of a bayonet tube would have some lateral support elements to mitigate its excessive bending. However, there is not sufficient information about this topic in the literature. Thus, a conservative analysis was considered in this work, where GPS conditions were employed in the interior tube of the bayonet tube, which leads to an upper limit on the thermal stress experienced by this tube. The mechanical properties of the tube material, obtained from [40], were modeled as temperature-dependent because, according to Laporte-Azcué et al. [55], the thermal stress is underestimated when the material properties are considered not to be temperature dependent.

5. Results and discussion

Through the CFD simulations of the models and the analytical methodology described in the previous sections, the impact of the eccentricity on the thermomechanical behavior of a bayonet tube was analyzed in this work. The results of this analysis are presented in the following subsections.

5.1. Velocity distribution

The hydrodynamic characterization of turbulent flow inside simple tubes has been thoroughly analyzed in the literature, [58–61] but less information can be found about bayonet tubes. Thus, this section is mainly devoted to analyzing the hydrodynamic behavior of the fluid inside the bayonet tube described in Section 2 for concentric and eccentric configurations. A description of the hydrodynamic behavior

of the molten salt inside the bayonet tube is provided via the contour maps of axial velocity (v_z), which are shown in Fig. 4. These contour maps, which were evaluated at different heights, were obtained for the concentric (Fig. 4(a)) and eccentric configurations of the bayonet tube (Fig. 4(b) and (c)) and for simple tubes (Fig. 4(d) and (e)). Since the flow in the annular section of the bayonet tube moves in the opposite direction of that in the circular section, the absolute value of axial velocity is represented in the figure. Overall, this figure illustrates that the velocity profile of the molten salt in both the annular and the circular passages barely changes with the axial coordinate, which demonstrates that the flow is hydrodynamically developed in most of the tube length and the variation of properties with temperature weakly perturbs the flow development. As mentioned, for the simulations carried out in this work, the cold molten salt enters the circular section ($z = 0$ m in Fig. 1) at 290 °C. After circulating through the interior tube, the molten salt returns through the annular section between the interior and the exterior tubes and exists at $z = 0$ m. The maximum velocity inside the internal tube is located at the tube axis, independent of the eccentricity of the bayonet tube. The reduced effect of the temperature dependence of the properties is observed in Fig. 4, in which the maximum velocity region of the circular tube increases slightly as molten salt is heated inside the tube. This effect is further discussed in the subsequent figures. The same behavior as discussed before for the interior tube of the bayonet tube is observed in the simple tube, where the maximum axial velocity is located at the tube axis and its magnitude is reduced gradually until reaching the tube walls. The highest simple tube, i.e., $D_e = 50$ mm achieves the lowest molten salt velocities since its mass flow rate was set to achieve a molten salt temperature increment of 37.6 °C. The smallest simple tube experiences fluid velocities similar to those obtained in the interior tube of the bayonet tube. The effect of the eccentricity in the molten salt flow is noticeable at the annular cross-section. In Fig. 4, a symmetric velocity distribution is observed in the concentric bayonet tube layout, where the axial fluid velocity is at the maximum level in the middle corona between the inner and outer tubes. This symmetric distribution is slightly broken at the front side of the annular passage at $z = 1$ m (i.e., close to the inlet and outlet of the tubes) because the heating of the molten salt diminishes the frictional force between the fluid and tube walls since the fluid density and viscosity are decreased. This fact causes a local acceleration of the flow in the cited zone, as can be observed in Fig. 4. For the eccentric layouts of the bayonet tube, the symmetry observed in the concentric configuration is clearly broken, generating a zone of maximum velocity at the front side of the tube where the gap between the interior and exterior tubes is at the maximum level ($\theta = 0^\circ$). At the rear of the bayonet tube ($|\theta| = 180^\circ$), this gap is reduced as eccentricity grows, which diminishes the cross-section locally. This fact produces a deceleration of the molten salt around $|\theta| = 180^\circ$ (see Fig. 4). This situation is unfavorable since this reduction in local velocity limits the convective heat transfer of the molten salt in this region.

To quantify the impact of the eccentricity and fluid properties on the axial velocity (v_z), the evolution along the tube length of the maximum velocity reached by the fluid at the circular and annular cross-sections is represented in Fig. 5(a) and (b). The maximum velocities are located at the center of the interior tube and at the widest region of the annular section. In the figure, the entrance region of the turbulent flow inside a circular cross-section duct can be observed, where the molten salt velocity at the tube's axis experiences constant growth until a peak is achieved. After this point, the velocity decreases, and its value stabilizes once the molten salt is fully hydrodynamically developed [62]. The overlapping of the curves in Fig. 5(a) reveals that the eccentricity does not sensibly affect the velocity distribution inside the interior tube as expected. Once the fluid is hydrodynamically developed in the interior tube ($z/d_i > 62.6$), the velocity profile does not appreciably change along the tube, although the velocity slightly increases (below 0.06%) due to fluid heating. A similar behavior appears in the axial velocity

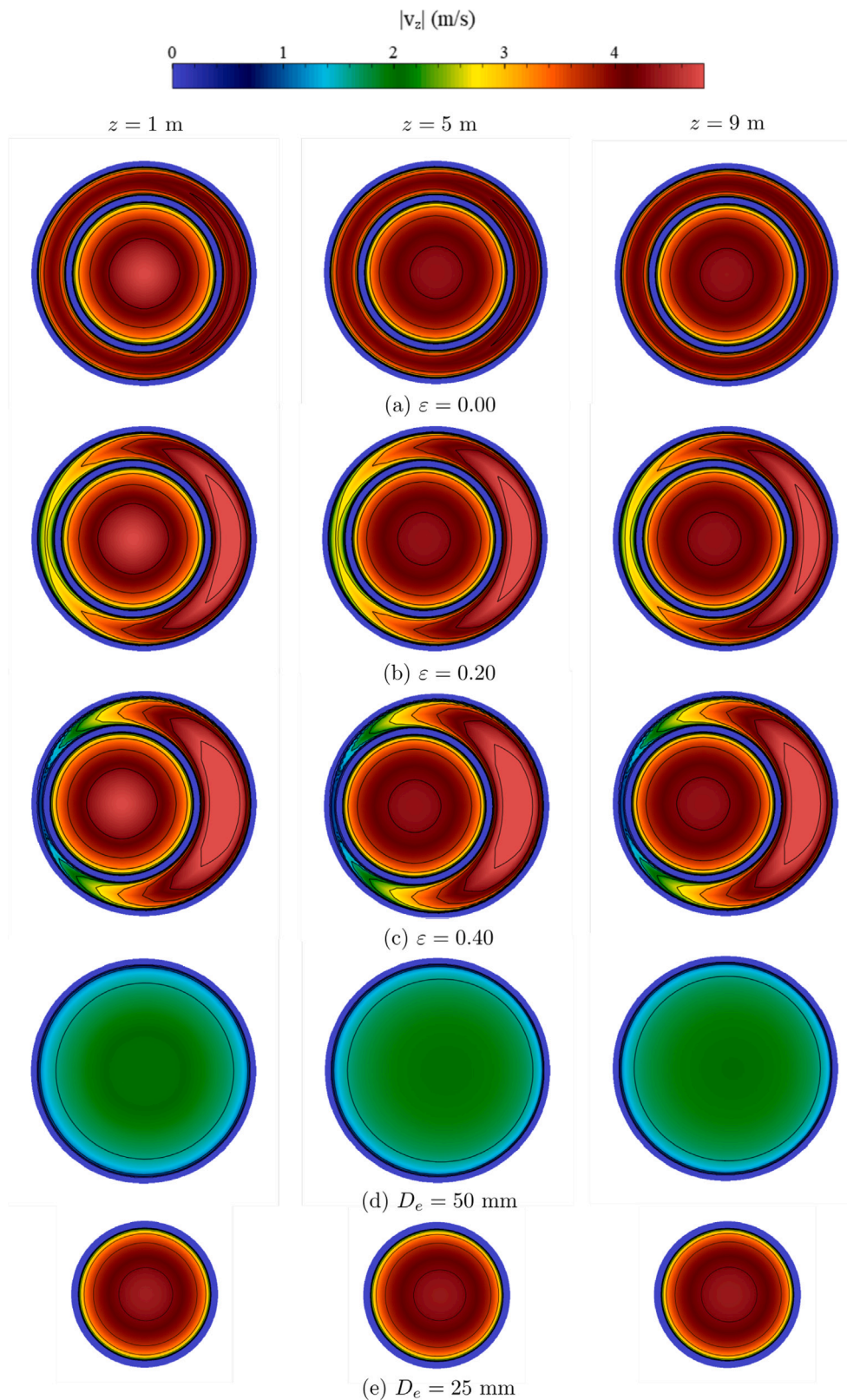


Fig. 4. Axial velocity contours obtained at different heights for (a) a concentric bayonet tube ($\xi = 0.00$), eccentric bayonet tubes with (b) $\xi = 0.20$, (c) $\xi = 0.40$, and simple tubes with (d) $D_e = 50$ mm and (e) $D_e = 25$ mm.

of the flow inside simple tubes (not shown here for simplicity) but with different magnitudes because, as mentioned above, the mass flow rate in the simple tube was modified to obtain the same temperature increment of the molten salt inside the tube in all cases. Thus, in the

fully developed region, the maximum velocities in the simple tubes for the highest ($D_e = 50$ mm) and smallest ($D_e = 25$ mm) tube diameters are 2.19 and 4.78 m/s, respectively. The end cap of the bayonet tube blocks the exit of the fluid at this section and connects the flow of the

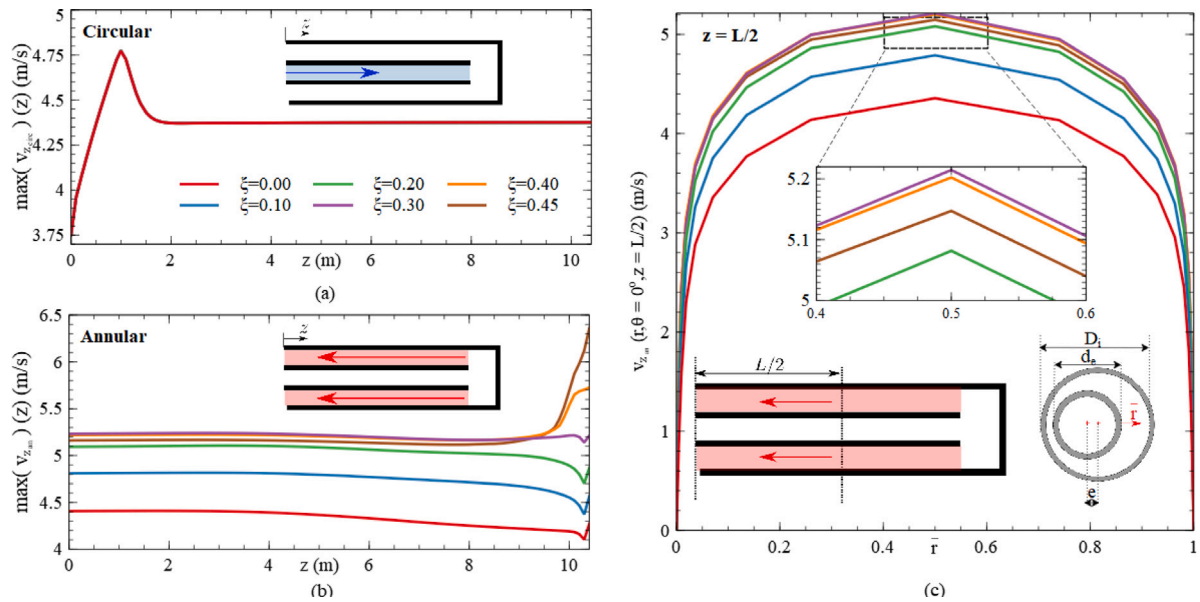


Fig. 5. Longitudinal evolution of the maximum axial molten salt velocity of several eccentricities reached at: (a) circular and (b) annular cross sections; (c) distribution of local axial velocity along the transversal position evaluated at the mid length of the tube ($z = L/2$) for several eccentricities.

interior tube with the annular passage. Then, the fluid after the annular duct inlet ($z \approx 10.49$ m) produces new thermal and hydrodynamic development. The hydrodynamic entrance can be observed in Fig. 5(b) as the zone where the axial velocity continually changes at the top of the tube ($z > 9.25$ m). From the results presented in this figure, it can be concluded that the hydrodynamic entrance length increases with eccentricity, as reported by Jonsson and Sparrow [25]. Once the fluid is hydrodynamically developed ($(L-z)/D_h > 60.2$), the maximum velocity of the fluid in the annular section grows slightly due to the decrease in its density. The maximum increment of velocity associated with this effect is 5.1%, which is achieved at the concentric configuration ($\xi = 0.00$) since it experiences the highest density variations due to its temperatures being the highest. As will be demonstrated later, eccentric layouts reach lower local temperatures at the front side of the tube than the concentric configuration, leading to a softer acceleration of the fluid since the molten salt density does not change substantially. For lower eccentricities ($\xi \leq 0.1$), the axial velocity at the tube's outlet increases by approximately 9.1% compared with the concentric configuration, while for larger eccentricities, this increase is as high as 18.6%. Eccentricities ranging between 0.2 and 0.45 do not create a significant variation in the maximum velocity at the tube's outlet (viz. variation below 2.8%).

The profiles of axial molten salt velocities at $\theta = 0^\circ$ in the annular section are presented in Fig. 5(c) for concentric and eccentric configurations of the bayonet tube. In the cited figure, the fluid velocity is represented along the radial direction in the gap between the interior and exterior tubes at $\theta = 0^\circ$. Since the gap in this region grows with the eccentricity, a normalized radial position ($\bar{r} = \frac{r-(e-r_e)}{R_i-(e-r_e)}$) has been defined. The normalized radial position ranges between 0 and 1, where $\bar{r} = 0$ is at the outer surface of the interior tube and 1 is at the inner surface of the exterior tube. To characterize the impact of eccentricity on the velocity profile, the different configurations of the bayonet tube were evaluated at the same height ($z = L/2$). As mentioned, the effect of the eccentricity is noticeable in the widest region of the annular passage at $\bar{r} = 0.5$, where the effect of the tube walls on the molten salt is less noticeable. If the axial velocity profile was expressed in dimensionless form, an overlap of the curves would be observed, agreeing with the velocity profiles obtained experimentally by Nouri et al. [27].

As discussed by Bradshaw [63], the Reynolds-stress gradients may generate vertex flows. In particular, the anisotropy of the Reynolds

stress caused by the annular cross-section of the bayonet tube induces a secondary motion, which is composed of a pair of vortices on each side of the symmetry plane [64]. These vortices transfer the momentum of the fluid from the broad front side of the section, where the momentum is high, to the narrow gap located at the rear. The fluid momentum is transferred through the midline of the gap, and then it returns through the duct walls. This phenomenon was numerically obtained by Nikitin et al. [35] and experimentally obtained by Nouri et al. [27].

5.2. Pressure drop

A beneficial effect of the eccentricity bayonet tube is the pressure drop reduction as eccentricity rises. This phenomenon has been reported and discussed in the literature through numerical and experimental analyses [22,23,25,31,35]. This reduction in the pressure drop is due to the decrease in the friction factor in the annular passage, which can be calculated according to Eq. (2) as a function of the longitudinal pressure gradient (dP/dz), hydraulic diameter (D_h), molten salt density (ρ) and fluid bulk velocity (u_b).

$$f = \frac{(-dP/dz)D_h}{\frac{1}{2}\rho u_b^2} \quad (2)$$

The pressure drop of the bayonet tube is the result of the contributions of the annular and circular passages and the end cap. To further understand the contribution of each zone to the total pressure drop, the pressure drop generated in each zone is summarized in Table 3 as a function of the eccentricity. The pressure drop in the inner tube, ΔP_{circ} , remains practically constant with eccentricity, at approximately 0.85 bar, which represents 26.6% of the total pressure drop of the concentric bayonet tube. As mentioned before, the total pressure drop is reduced with eccentricity. Thus, the contribution to the pressure drop of the circular cross-section rises to 29.3% for the most eccentric configuration studied in this work ($\xi = 0.45$). An increase in the pressure drop at the end cap, ΔP_{cap} , is observed as the eccentricity rises. For large eccentricities, the pressure drop in the cap increases approximately two times compared with the concentric configuration, rising from 0.15 bar in the concentric configuration to 0.30 bar at $\xi = 0.45$. The contribution of the end cap to the total pressure drop ΔP_{total} ranges between 4.2% and 10.4%. When the eccentricity rises, i.e., the interior tube is moved to the rear side of the exterior tube, an augmentation of the local velocity is observed, which would augment the pressure drop at the

Table 3
Pressure drop obtained in the simple tube and bayonet tube and the contribution of each component to the pressure drop as a function of the eccentricity.

Type	D_e (mm)	ξ	Circular ΔP_{circ} (bar)	Annular ΔP_{an} (bar)	Cap ΔP_{cap} (bar)	Total ΔP_{total} (bar)
Bayonet	50	0.00	0.85	2.61	0.15	3.61
		0.10	0.85	2.55	0.15	3.55
		0.20	0.85	2.43	0.16	3.44
		0.30	0.85	2.22	0.17	3.24
		0.40	0.85	1.95	0.21	3.01
		0.45	0.85	1.77	0.30	2.92
Simple	50	–	0.13	–	–	0.13
	25	–	1.28	–	–	1.28

annular section (ΔP_{an}). Nevertheless, the diminution of f compensates for this fact, resulting in a reduction in the pressure drop at the annular passage as eccentricity grows. The concentric configuration achieves an annular pressure drop of 2.6 bar, which is reduced by approximately 30.8% in the largest eccentric configuration (i.e., $\xi = 0.45$). Due to the configuration of the bayonet tubes, the molten salt would traverse two times more distance than in simple tubes. In addition, it is necessary to add the pressure loss of the end cap. The pressure drops of the simple tubes, used as a reference, have been computed, and their values are included in Table 3. These pressure drops are approximately 0.13 bar and 1.28 bar for the largest and smallest tube diameters, respectively. Therefore, the minimum pressure drop of bayonet tubes is almost 2.28 and 22.46 times higher than that obtained in the smallest and highest simple tubes, respectively (i.e., 25 and 50 mm)

5.3. Temperature distribution

The influence of eccentricity on the hydrodynamic behavior of the bayonet tube, which was discussed in the previous section, is reflected in the temperature of the molten salt and the tube, as observed in the contour maps of Fig. 6. These contour maps, which are evaluated at different heights, have been obtained for concentric (Fig. 6(a)) and eccentric configurations of bayonet tubes (Fig. 6(b) and (c)). For comparative purposes, the contour maps of both simple tubes are represented in Fig. 6(d) and (e). As noted, the configuration of the external tubular receiver causes the absorbed heat flux to have a nonuniform distribution, which leads to the thermal field. As shown in Fig. 6, the temperature distribution of the exterior tube has the highest temperature gradients since the incident heat flux hits directly over its surface, while the interior tube temperature is more homogeneous because the tube is mainly heated by the surrounding molten salt. This fact attenuates the thermal gradients experienced by the interior tube. Thus, the tubes of the bayonet tube, i.e., the interior and exterior tubes, do not have the same behavior since they are not subjected to the same conditions. The maximum difference between the molten salt temperatures in annular and circular passages is located close to the inlet/outlet of the duct since due to the bayonet tube layouts, the cold molten salt arrives through the interior tube while the hot fluid exits the tube through the annular passages at the same position. As the molten salt is pushed toward the top of the bayonet tube, the temperature difference between the fluid in the annular and circular passages is progressively diminished, as illustrated in Fig. 6. For the simple tube, Fig. 6(d) and (e), a more uniform temperature distribution is observed in the molten salt, which is progressively heated as it flows inside the tube. In the largest simple tube, the wall temperatures are considerably higher than those obtained in the bayonet tubes or the smallest simple tube.

As previously discussed, due to the eccentricity, the fluid velocity is enhanced near the most thermally demanding zone, $\theta = 0^\circ$, leading to a reduction in the maximum exterior tube temperature. Independent of the eccentric configuration, the maximum temperatures are located at the outer tube surface, at a location near to where the heat flux peaks. Despite the promising effect caused by the eccentricity at the front of

the tube, another unfavorable effect is produced in the rear, where the interior tube partially prevents heat transfer from the front to the rear of the annular cross-section. The temperature distribution achieved in the rear of the annular passage ($|\theta| > 100^\circ$) is similar to those reached at the circular passage. The backside temperature of the annular section barely changes along the tube length, as will be demonstrated in the next figures. This effect is accentuated as eccentricity enlarges. Thus, the eccentric configuration contributes to reducing the maximum tube temperature, although it impedes the greatest amount of heating in the rear of the annular cross-section. According to [65], the thermal stresses of the tube are related to the nonuniformity in the tube wall temperature. Therefore, it is difficult to define which of the effects is dominant over the thermal stresses. Therefore, mechanical analysis is needed to unveil whether the eccentricity may reduce the thermal stresses.

Through the axial evolution of the bulk temperature of molten salt and the temperature distribution at the surface of both interior and exterior tubes, it is possible to quantify the impact of the eccentricity on the temperature field analyzed in Fig. 6. The bulk temperature of the molten salt in Section A is computed, as shown in Eq. (3), by weighting its local temperature with its local properties as the density (ρ_{salt}), specific heat ($C_{p,salt}$) and axial velocity (v_z). This equation is applied for the annular and circular cross-sections of the bayonet tube and for the circular section of the simple tube.

$$\bar{T} = \frac{\int_A \rho_{salt} C_{p,salt} v_z T_{salt} dA}{\int_A \rho_{salt} C_{p,salt} v_z dA} \quad (3)$$

The axial evolution of the bulk temperature of the molten salt at both annular and circular passages is shown in Fig. 7 for several eccentricities. For comparative purposes, the axial evolutions of the molten salt bulk temperatures of the two simple tubes ($D_e = 50$ mm and 25 mm) are represented as black solid lines in the cited figure. However, the two curves overlap because both simple tubes have the same heating rate conditions. As described before, the cold molten salt flows first through the interior tube, where its temperature progressively increases due to the heat absorbed from the annular passage. The bulk temperature at the interior tube of the bayonet tube is depicted as dashed lines in the figure. Once the molten salt arrives at the top of the tube, the end cap changes the flow direction, so the molten salt flows back through the annular section (represented as solid lines), where the heating rate is more accentuated than that of the interior tube. For the concentric configuration, the molten salt temperature in the interior tube grows by 4.4 °C, while this increase in temperature is reduced to 2.6 °C for the largest eccentric configuration studied in this work ($\xi = 0.45$). This reduction in the temperature increment is provoked by the augmentation of the separation between both the interior and exterior tubes. This causes more molten salt to locally flow between tubes, absorbing the heat that would have been absorbed by the interior tube with lower eccentricity. Based on these results and due to the relatively low-temperature increase in the inner tube, the numerical model of the bayonet tube could be simplified by analyzing only the annular passage and substituting the flow of the molten salt in the interior tube by an average temperature and an overall

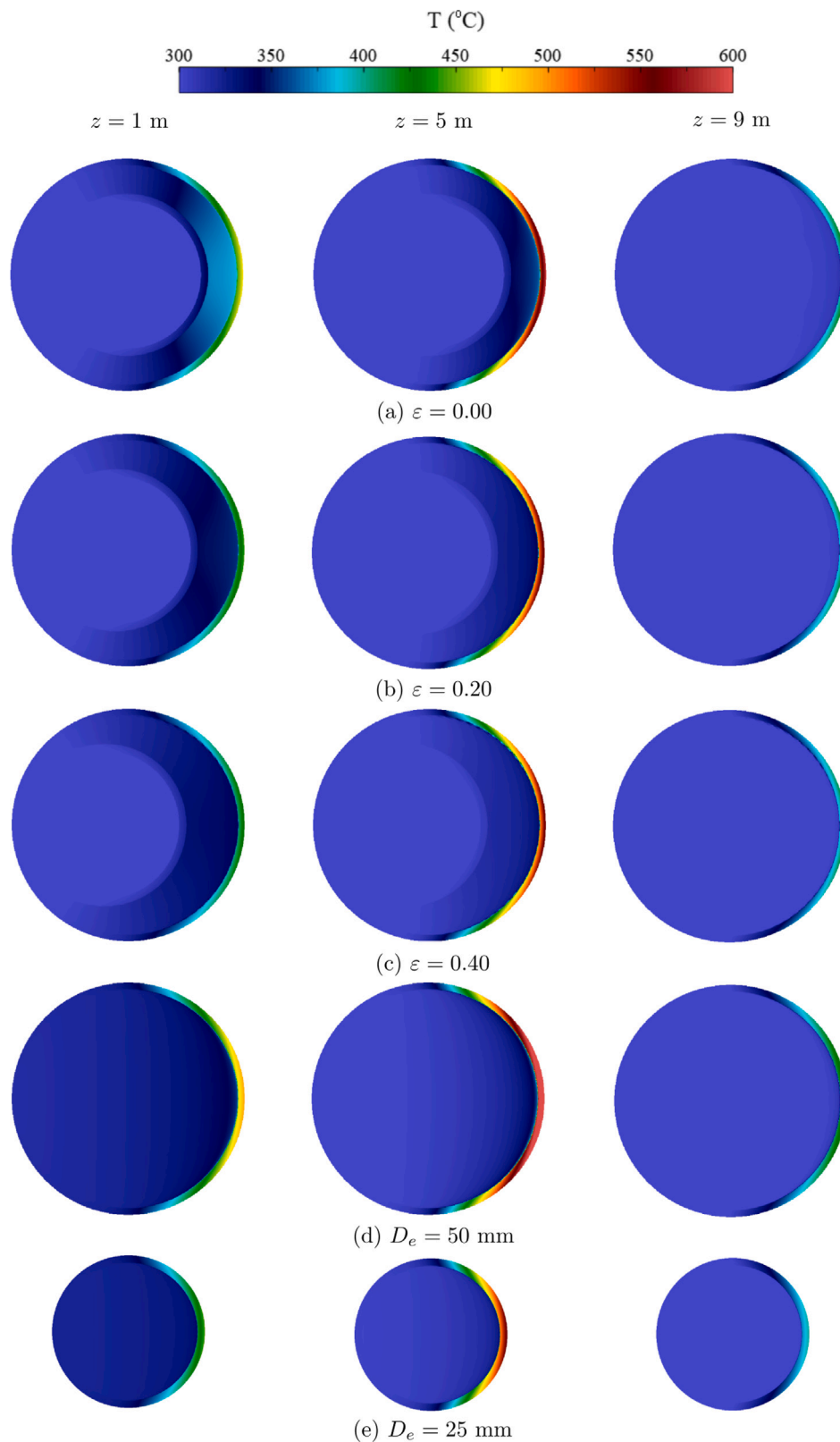


Fig. 6. Temperature contour maps obtained at different heights for the (a) concentric bayonet tube ($\xi = 0.00$), eccentric bayonet tubes (b) $\xi = 0.20$, (c) $\xi = 0.40$, and simple tubes: (d) $D_e = 50$ mm and (e) $D_e = 25$ mm.

heat transfer coefficient. This simplification was employed in other works, such as [64,66,67], where only the molten salt flow in the annular passage was analyzed. Nevertheless, for other fluids, such as liquid metals, it would be necessary to examine the validity of this

simplification. Although the temperature increment of the molten salt inside the absorber tube is the same for all the cases analyzed in this work, the local absorbed heat rate differs along the tube length due to the different conditions experienced by the fluid inside the eccentric

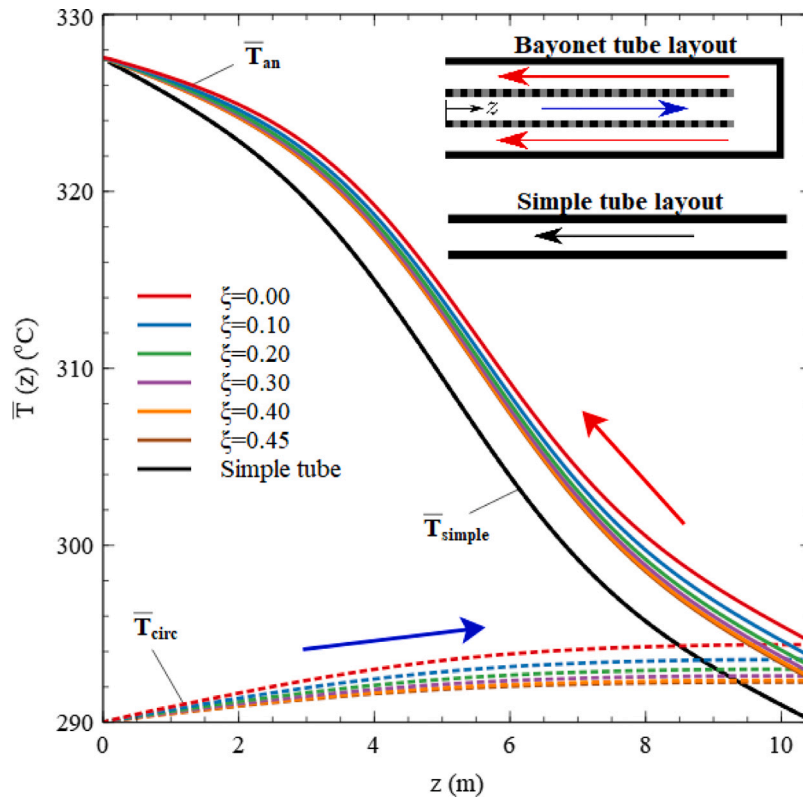


Fig. 7. Axial evolution of the molten salt bulk temperature for several eccentricities of bayonet tubes and for simple tubes. Solid lines: Bulk temperature in the annular passage. Dashed lines: Bulk temperature in the circular passage. Black solid lines: Simple tubes.

bayonet tube. In light of the results presented in the figure, the eccentric configurations can achieve a higher temperature increase per meter than concentric bayonet tubes, indicating that the thermal performance of the bayonet tube is enhanced with eccentricity. For the conditions studied in this work, the simple tubes experience higher temperature increments, since the molten salt temperature grows 37.6 °C in 10.5 m, while inside the bayonet tube, the HTF needs to flow inside both the circular and annular passages to achieve this increment.

The axial and circumferential temperature distributions of the exterior and interior tubes are depicted in Figs. 8 and 9, respectively. These figures illustrate the temperature distributions of the inner and outer surfaces of both the interior and exterior tubes. First, the axial temperature evolutions of exterior tubes are represented in Fig. 8(a) and (b) for several eccentricities. The axial evolution of the exterior tube temperature is directly related to the absorbed heat flux distribution, which is higher near the mid-axial position and depends on the aiming strategy of the heliostat field. The maximum temperature, named the peak temperature here, is located on the outer surface of the exterior tube at $\theta = 0^\circ$. In Fig. 8(a), the axial evolution of the outer tube surface is represented for both simple and exterior bayonet tubes. For the concentric configuration of the bayonet tube, $\xi = 0$, the peak temperature is achieved at $z \approx L/2$, and it has a value of 595.5 °C. This value is reduced above 132 °C when the position is close to the extreme sides of the tube (i.e., $z = 0$ m and 10 m) since, in these zones, the incident radiation is considerably diminished. Independent of the eccentricity, the top of the tube ($z = L$) reaches the lower peak temperature, i.e., below 400 °C, since the cooling of the tube walls is enhanced due to the capability of molten salt to store more heat when it has a lower temperature. The increase in the molten salt velocity at the front of the annular cross-section generated by eccentricity causes an improvement in the cooling of the exterior tube walls at $\theta = 0^\circ$, reducing their temperatures. Compared with the concentric configuration of the bayonet tube, the smallest eccentricity studied in this work, $\xi = 0.1$, reduces the maximum tube temperature

by approximately 2.4%, while for one of the largest eccentricities, $\xi = 0.45$, this reduction increases until 4.9%, which represents a decrease of 29.4 °C in the maximum tube temperature. In addition, the influence of eccentricity is clearly observed at $z = 0$ m, where the eccentricity decreased until 8.1%, which is the temperature reached at the same point for a concentric configuration, passing from a peak temperature of 463.2 °C for $\xi = 0$ to a temperature of 425 °C for $\xi = 0.45$. The axial evolutions of the simple tube temperatures are similar to those experienced by the bayonet tubes. The peak temperature is located at the middle of the tube at 664.1 °C and 569.4 °C for the largest and smallest tube diameters, respectively. This fact implies that an eccentric bayonet tube could achieve a lower peak temperature than a simple tube with half the diameter. Although these temperature reductions might seem insignificant, they could lead to an essential difference in the creep damage of receiver tubes. The simple tube with the largest external diameter (i.e., $D_e = 50$ mm) has a larger peak temperature than the concentric or eccentric bayonet tubes. In Fig. 8(b), the axial evolution of the inner tube surface is represented for both simple and exterior bayonet tubes. This surface experiences lower temperatures than those achieved at the exterior surface. Analogous to the exterior tube surface, the highest temperature (522.7 °C) is obtained in the middle of the tube for the concentric configuration, while for $\xi = 0.45$, this temperature might be reduced to 490.5 °C. For the highest and smallest simple tubes, the temperatures on these surfaces are 597.9 °C and 506.4 °C, respectively. In Fig. 8(c) and (d), the circumferential distributions of the temperatures of both the outer and inner surfaces of the exterior tube are shown for several eccentricities. These curves are evaluated at $z = L/2$ from the tube inlet, since the maximum temperature is located at (or very close to) this position. As mentioned above, due to the receiver configuration, one part of the tube faces the heliostat field, while the other part faces the radiant wall. For this reason, the maximum temperature of the exterior tube is located at the front of the outer surface ($\theta = 0^\circ$), while the minimum temperature is located in the rear ($|\theta| = 180^\circ$), as shown Fig. 8(c). The circumferential

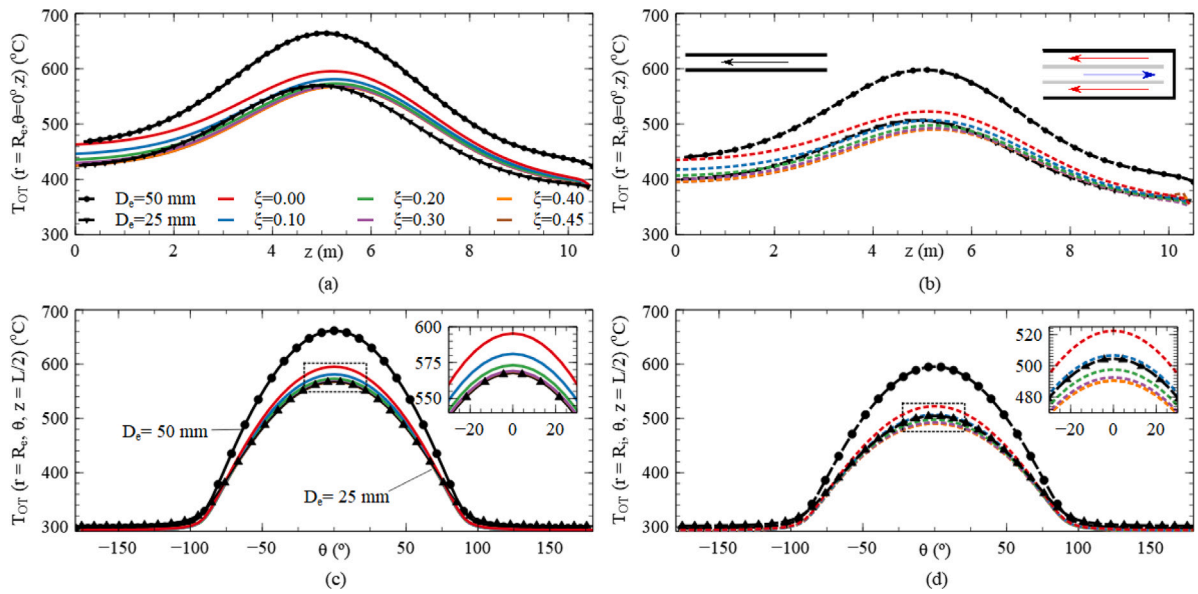


Fig. 8. Wall temperature distributions of the exterior tubes of concentric ($\xi = 0$) and eccentric bayonet tubes ($\xi > 0$): Axial distribution of the maximum temperature achieved in the tube of (a) the outer surface and (b) the inner surface. Circumferential distribution of the tube temperature of the (c) outer surface and (d) inner surface. Solid lines: outer tube surface. Dashed lines: inner tube surface. Black lines with bullets: simple tube.

profile of the absorbed heat flux leads to the nonaxisymmetric temperature distribution. The behavior described for the axial variation of the maximum temperature is extrapolated to the whole front section of the tube, $|\theta| < 75^\circ$. The influence of eccentricity is noticed in the front section for $|\theta| < 50^\circ$, although its effect is more notable at $\theta = 0^\circ$. As can be observed in Fig. 8(d), the behavior of the inner tube surface is similar to that described for the outer surface.

The largest temperature difference between the inner and outer surfaces of the interior tube, whose temperatures are represented in Fig. 9(a), is located, independent of the eccentricity, at $z = 0$ m (viz., tube inlet and outlet). This fact is due to the cold molten salt arriving through the circular cross-section while the hot molten salt exits the bayonet tube through the annular cross-section at this point. As the axial position moves to the interior tube top, the temperature variation between the inner and outer tube surfaces is reduced, achieving a uniform temperature distribution at the tube's top. Thus, the maximum thermal gradient of the interior tube is located at the tube's inlet/outlet for $\xi = 0.0$, where the temperature difference between tube surfaces is 16.1°C . The concentric configuration also achieves the highest temperature on the exterior surface, 344.1°C , while this value is reduced by 7.5% as eccentricity rises until 0.45. The curves of the circumferential distribution of the interior tube temperature are shown in Fig. 9(b). As mentioned before, the largest temperatures are obtained on the outer surface of the tube in a concentric layout, whose temperature varies from 325°C at $\theta = 0^\circ$ to 293.9°C at $|\theta| = 180^\circ$. The more eccentric layout analyzed in this work, $\xi = 0.45$, reduced the maximum temperature of the concentric case by approximately 5.8%, while at the rear of the tube, this difference was below 2°C . Independent of the eccentricity, above $|\theta| > 160^\circ$, the temperature curves of both surfaces overlap.

5.4. Convection heat transfer

The convective coefficient of the molten salt in the outer tube of the bayonet tube was obtained using Newton's law of cooling and the results of the CFD simulations. Namely, the Nusselt number was calculated (see Eq. (4)) as a function of the bulk temperature of the molten salt at the cross-section ($\bar{T}(z)$), the film temperature of the HTF at the inner surface of the tube ($T(r = D_i/2, \theta, z)$), the absorbed heat flux ($q''_{abs}(r = D_i/2, \theta, z)$), the characteristic length, which is equal to

hydraulic diameter of the annular passage of bayonet tube (D_h) and it is equal to the inner diameter for simple tube, and the thermal conductivity of molten salt (k_{salt}) evaluated at $\bar{T}(z)$.

$$Nu(\theta, z) = \frac{D_h}{k_{salt}} \left(\frac{q''_{abs}(r = D_i/2, \theta, z)}{T(r = D_i/2, \theta, z) - \bar{T}(z)} \right) \quad (4)$$

Fig. 10(a) shows the axial evolution of the Nusselt number of the simple tubes (Nu_{circ}) and the Nusselt number of the exterior tubes of the annular passages (Nu_{an}) of the bayonet tubes. All these curves are evaluated at $\theta = 0^\circ$ for several eccentricities. From a qualitative point of view, the axial evolution of the convection coefficient at $\theta = 0^\circ$ of both simple and bayonet tubes depends on the relation between the temperature distribution and the absorbed heat flux. In the first half of the tube ($0 < z < L/2$), the heat transfer coefficient increases until it reaches a maximum near the middle of the tube, while after this point and extending to the top of the tube, the convection heat transfer slightly decreases. This axial variation of the Nusselt number is mainly caused by the axial distribution of the incident heat flux. Nevertheless, when the incident heat flux is reduced (i.e., at the extreme sides of the tube), other parameters that might affect the convection appear, such as the increase in the fluid velocity or the heating of the tube. As the heat rates are set to be equal (viz. heat flux distribution, employed to simulate the solar radiation reflected by the heliostat field, and the dimensions of the tube are identical for each simulation), the difference in the heat transfer coefficient between cases is caused by the eccentricity. The convection coefficient increases with eccentricity due to the rise in the local molten salt velocity, leading to an increase in the flow turbulence and improving the cooling of the tube walls of the annular section. The eccentricity increases the heat transfer coefficient of the concentric bayonet tube configuration to 26.1% (the value achieved at the largest eccentricity studied in this work). Nevertheless, the Nusselt number can camouflage the real nature of the heat transfer since it weighs the local heat transfer coefficient with the characteristic length. This fact justifies why the simple tubes have the largest Nusselt number despite their tube temperatures being higher than those obtained in bayonet tubes. If the heat transfer coefficient was graphically represented, it could be observed that the bayonet tube achieves the largest values, demonstrating a better tube wall cooling effect in bayonet tubes.

The circumferential distribution of the Nusselt number evaluated at $L/2$ is shown in Fig. 10(b) for both simple and bayonet tubes. The

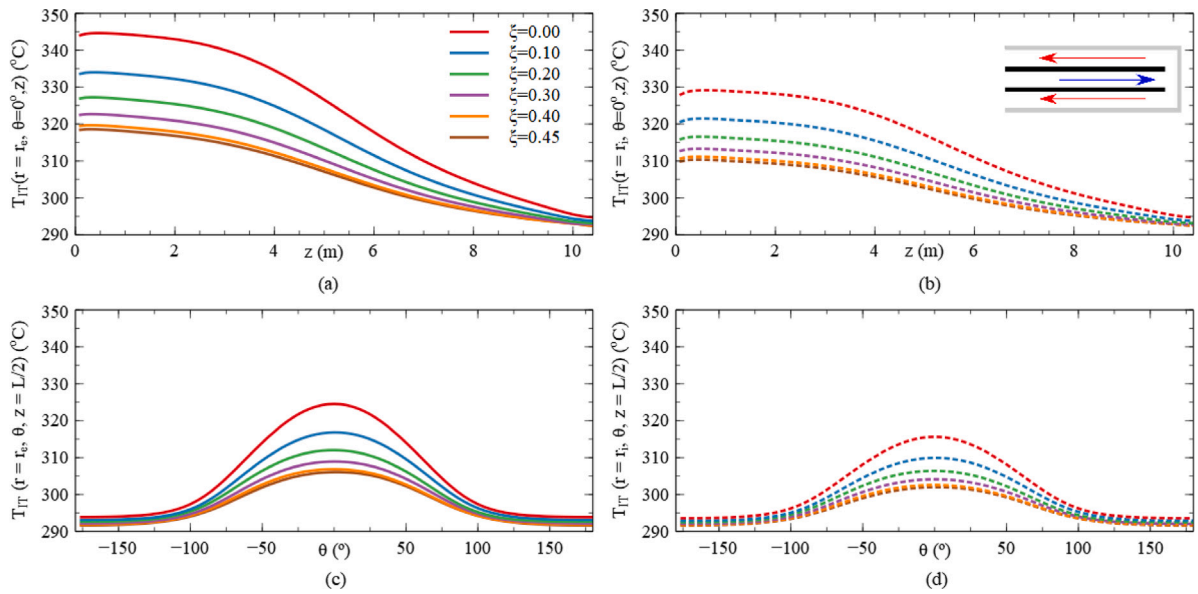


Fig. 9. Wall temperature distribution in the interior tube of concentric ($\xi = 0$) and eccentric bayonet tubes ($\xi > 0$): Axial distribution of the maximum temperature achieved in the tube of (a) the outer surface and (b) the inner surface. Circumferential distribution of the tube temperature of the (c) outer surface and (d) inner surface. Solid lines: outer tube surface. Dashed lines: inner tube surface.

following three zones can be observed in the circumferential distribution of the Nusselt number: (i) positive and nearly constant values of the Nusselt number, where the local film temperature is higher than the bulk temperature ($|\theta| < 75^\circ$), (ii) an asymptotic zone where the local film temperature is close to the bulk temperature ($75^\circ < |\theta| < 110^\circ$) and (iii) a region where the local film temperature is lower than the bulk temperature ($|\theta| > 110^\circ$). The discontinuity and the negative values of the local convective coefficient are due to the use of the traditional definition of the heat transfer coefficient, Eq. (4), under a nonuniform temperature distribution. Those points where the temperatures of the fluid and the inner tube surface are similar reflect a discontinuity in the distribution of the local convection coefficient. This discontinuity in the Nusselt number is a mathematical artifact and does not represent a discontinuity in the convection heat transfer inside the tubes. The angular position where the convective coefficient asymptote is located depends on the circumferential shape of the heat flux. The influence of the eccentricity is more notable at $|\theta| < 50^\circ$ (i.e., the front side of the tube). As explained above, when the interior tube is moved to the rear, the symmetric distribution of the molten salt velocity is broken, generating a high-velocity zone near the zone with the highest thermal demand. This fact is observed in the circumferential distribution of the heat transfer coefficient, where it is enhanced as the local velocity increases due to the eccentricity. In addition, the Nusselt numbers provided through different experimental correlations are included in Fig. 10(b) as a reference. These correlations are (i) Dittus–Boelter [68], which is one of the most popular experimental correlations devoted to characterizing the convection heat transfer of turbulent flows inside ducts, (ii) Monrad and Pelton [54], which was developed for turbulent flow in smooth concentric annular ducts, and (iii) Serrano et al. [30], which provided a correlation to compute the local convection heat transfer for a turbulent air flow inside an eccentric annular duct ($\xi = 0.44$). Experimental Nusselt numbers, represented as gray dotted lines in the figure, have been computed from the temperature field and absorbed heat flux obtained from the CFD simulation of the bayonet tube. Only good agreement between the experimental correlation and results obtained through simulations is observed at $|\theta| < 75^\circ$ due to the nonuniformity of the heating conditions. The Dittus–Boelter and Monrad–Pelton correlations only provide good agreement with the Nusselt number of the concentric configuration, although the Reynolds and Prandtl numbers are similar

for all bayonet layouts. The correlation provided by Serrano et al. [30] captures the enhancement of the convection heat transfer at $\theta = 0^\circ$, although it overestimates its value. This overestimation may be because the correlation was developed from measurements with air and then corrected for other fluids. This reveals the need to continue working to develop experimental correlations devoted to characterizing the convection heat transfer of eccentric annuli.

5.5. Thermal stress

Finally, thermal stresses were calculated using the methodology proposed by Laporte-Azcué et al. [55]. As mentioned above, the thermal stress is directly related to the nonuniform distribution of temperature inside the tube walls [65,69]. This temperature distribution causes the thermal expansion between the front and rear sides of the tube to be different, which is translated into tube bowing. Due to thermal expansion of the tube, partially restricted by clips, the following two zones are differentiated as a function of the axial stress response of the tube: compression ($\sigma_z < 0$) and traction ($\sigma_z > 0$) zones. The minimum value of axial stress is located on the outer surface at the front, while the maximum axial stress is achieved in the rear of the tube. The compression stress reached at the front of the tube is more than 6 times higher than the other stress components. The equivalent von Mises stress (σ_{VM}) is used to consider all stress components in the mechanical analysis. The von Mises stress inside the tube walls is shown in Fig. 11 for both the interior and exterior tubes of the bayonet tubes and for simple tubes. Similar to previous contours, these contour maps have been obtained for concentric (Fig. 11(a)) and eccentric configurations of bayonet tubes (Fig. 11(b) and (c)) and for both the largest and smallest simple tubes (Fig. 11(d) and (e)). These contours are evaluated at different heights. From these contour maps, it can be asserted that the exterior tube of the bayonet tube is the most demanding tube from a mechanical point of view. In addition, the largest simple tube achieves the largest thermal stresses, while the stress distribution of the smallest simple tube is analogous to those obtained in eccentric bayonet tubes. From a qualitative point of view, the von Mises stress achieved in the tube walls can be organized into the following three regions: (i) the zone with maximum stress (located at the front side), (ii) zone with values close to 0 (located at $|\theta| \approx 75^\circ$) and (iii) zone with a uniform distribution of σ_{VM} at the rear. The effect of the eccentricity is also

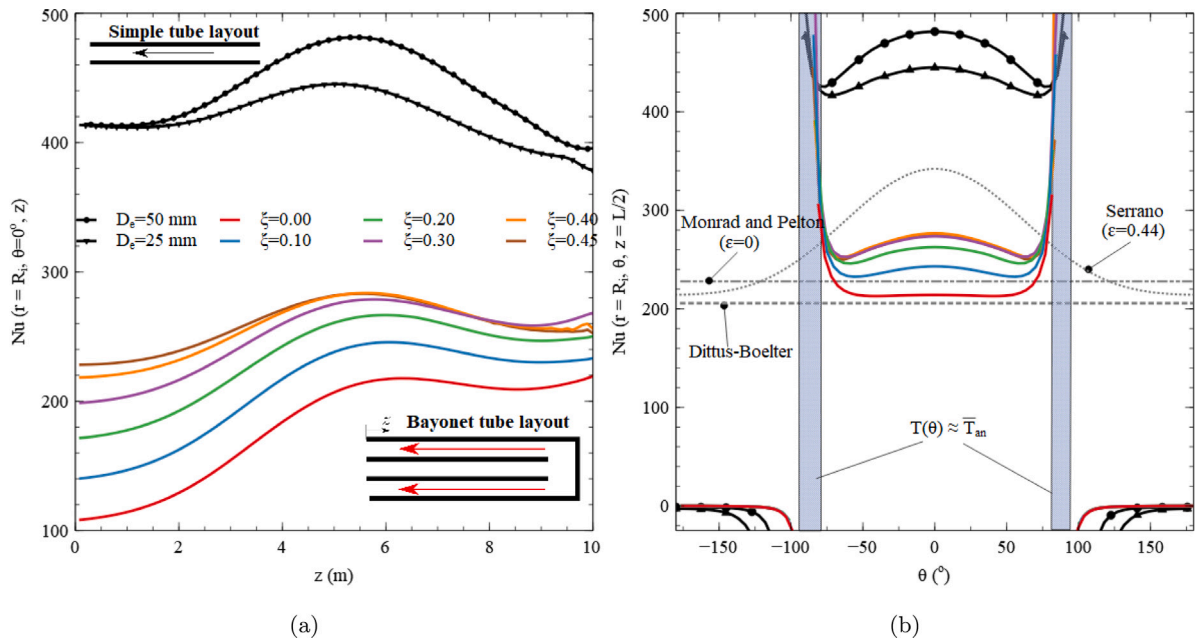


Fig. 10. Nusselt number obtained at the inner surface of the exterior tube for several eccentric configurations and at the inner surface of simple tubes. (a) Axial evolution at $\theta = 0^\circ$, (b) circumferential distribution evaluated at $z = L/2$ from the tube inlet.

observed in the stress distribution. The reduction of stress is mainly observed at the front, where the impact of eccentricity on the molten salt and tube temperatures is more notable. The stress peaks at the same point where the temperature and the incident heat flux are highest. The maximum stress distribution of the exterior tube is approximately 9 times higher than those achieved in the interior tube. For both tubes of the bayonet tubes, the outer surface is the most demanding zone. For this reason, in the next figures, only these surfaces have been reported and compared with the equivalent stress obtained in simple tubes.

The axial evolution of the maximum von Mises stress, which is located at the front of the outer tube surface, is shown in Fig. 12(a) for several eccentricities and for both simple tubes. In this figure, the solid lines curves represent the von Mises stress on the outer surface of the exterior tube, while the dotted lines represent the stress of the outer surface of the interior tube. Through this figure, the effect of the eccentricity on the mechanical performance of the bayonet tube can be discussed. The axial shape of the incident heat flux is translated to the temperature and stress axial distributions of the exterior tube. For the purpose of this work, $k_{aim} = 3$, the sunlight concentration is at the maximum value at the half length of the tube and is progressively reduced at the extreme sides of the tube. As shown in the figure, when the eccentricity grows, the equivalent stress is diminished since the convection heat transfer is increased due to the HTF flowing faster in the zone of the tube with the most thermal demand, enhancing the cooling of the tube walls in this region. This fact reduces the nonhomogeneous temperature distribution and the consequent thermal stresses. For the interior tube of the bayonet tube, the nonhomogeneity of the temperature distribution grows as the position is close to the tube's inlet and outlet (i.e., $z = 0$ m), leading to an enlargement of σ_{VM} as z decreases. This is due to the configuration of the bayonet tube, which causes the largest variation in the interior tube temperature to occur at this position. At this point, the stress of the exterior tube is greater than 3.2 times the von Mises stress peak of the interior tube. As mentioned previously, for each configuration of the bayonet tube, the maximum stress is located in the exterior tube at the half-length of the tube, $z = L/2$. The highest equivalent stress is reached for the concentric configuration, 618.2 MPa, and it decreases by approximately 8.8% for the largest eccentricity case. For $\xi > 0.25$, the peak of equivalent stress barely changes, passing from 575.5 MPa at $\xi = 0.25$

to 563.7 MPa reached $\xi = 0.45$. The lowest value of the maximum equivalent stress is reached when $\xi = 0.4$. However, the improvement in the thermal stresses is lower than 0.1% compared with adjacent eccentricities (i.e., $\xi = 0.35$ and $\xi = 0.45$). The maximum equivalent stress, i.e., 736.3 MPa, is achieved at the simple tube with the same diameter as the external bayonet tube due to the combination of the following two factors: (i) the largest inertial moment associated with the tube diameter and (ii) the highest temperature. This value is 1.2 times higher than the peak stress achieved in a concentric bayonet tube. Despite the smallest simple tube experiencing a higher temperature than the eccentric bayonet tube, its inertial moment is lower than those obtained in the latter. Thus, its maximum stress is approximately 2.1% lower than the stress obtained in the most eccentric layout analyzed in this work. Fig. 12(b) illustrates the circumferential distribution of the von Mises stress evaluated on the outer tube surface for both the interior and exterior tubes of the bayonet tube. As discussed, independent of the bayonet tube layout, the maximum stresses are located at the front of the tube (facing the heliostat field). Although the stress achieved at the rear of the tube ($|\theta| = 180^\circ$) is lower, it cannot be neglected. The effect of the eccentricity is clearly observed on the tube surface, although its influence is more notable at $\theta = 0^\circ$. In the rear, the equivalent stress is stabilized from $|\theta| > 105^\circ$ for all the bayonet tubes studied. The concentric configuration achieves the highest stress, i.e., 293 MPa, while it is diminished by 8.0% with the largest eccentricity. Eccentricities above 0.2 lead to a similar stress distribution in the rear zone.

Although the peak stress of the smallest simple tube is lower than those obtained in the eccentric bayonet tube, its interaction with temperature may produce higher creep damage than that experienced by the bayonet tube. The methodology proposed [by González-Gómez et al. [70] has been used to characterize the time to rupture associated with creep damage (t_R) obtained during the operation of both the simple and the bayonet receiver tubes. The time to rupture, which depends on the tube temperature T in Kelvin and the effective creep stress σ_{eff}^{creep} in MPa is calculated from the following:

$$\log_{10}(t_R) = -26.27 + \frac{44158}{T} + 4.72 \log_{10}(\sigma_{eff}^{creep}) - \frac{11337}{T} \log_{10}(\sigma_{eff}^{creep}) \quad (5)$$

The coefficients of Eq. (5) were obtained by Eno et al. [71] for Haynes 230. As a first conservative approach, the effect of the stress relaxation was not considered so that the effective creep stress is equal to the

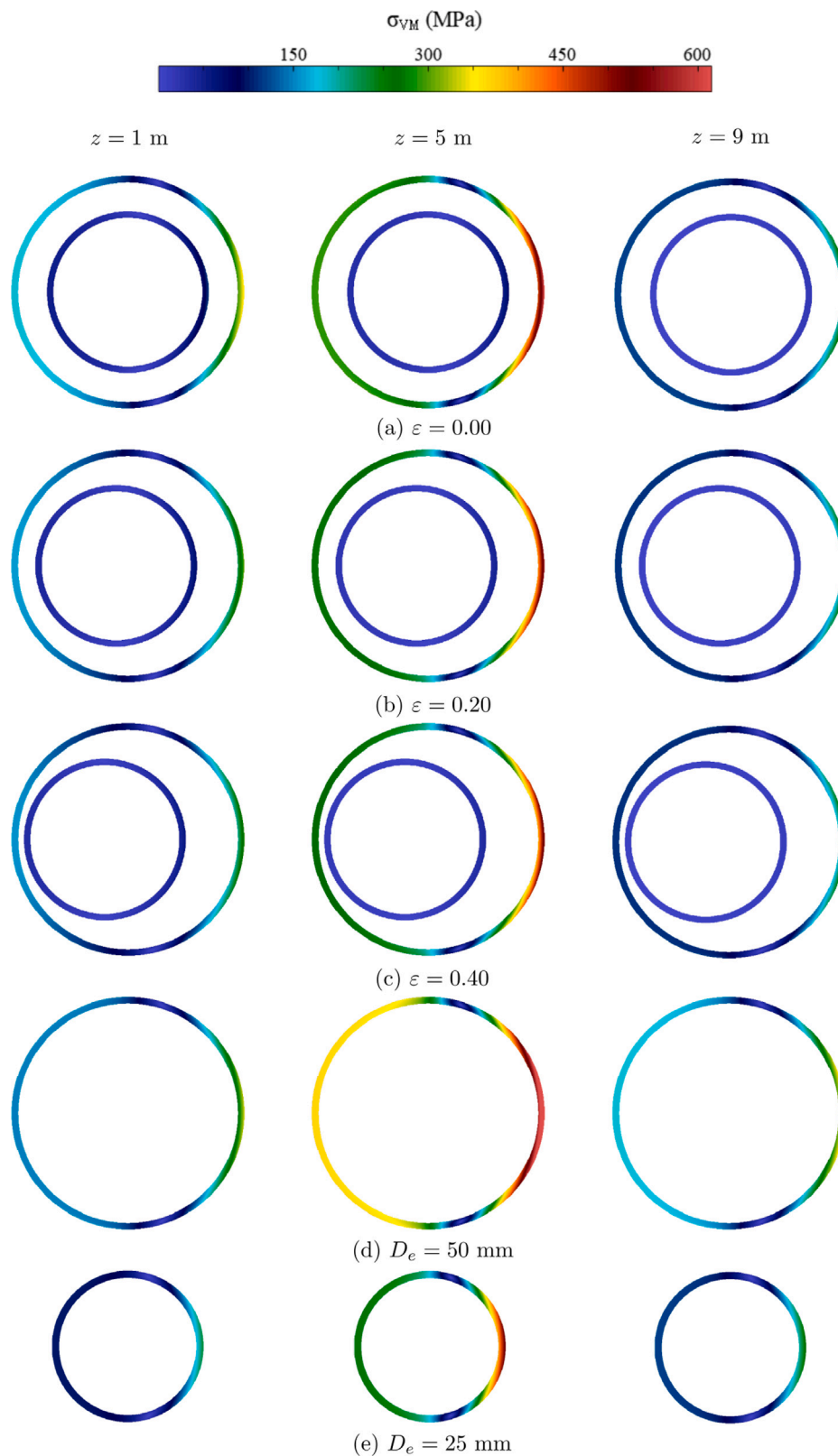


Fig. 11. von Mises stress contour maps obtained at different heights for (a) a concentric bayonet tube ($\xi = 0.00$); eccentric bayonet tube es: (b) $\xi = 0.20$, (c) $\xi = 0.40$; and simple tubes: (d) $D_e = 50$ mm and (e) $D_e = 25$ mm.

equivalent von Mises elastic stress ($\sigma_{eff}^{creep} = \sigma_{VM}$). As the exterior tube of the bayonet tube experiences the largest temperatures and thermal stresses, its time to rupture is lower than that of the interior tube. Through the above equation and using the values of the maximum

stress of the tube and the temperature of that point, the time to rupture can be estimated. Table 4 shows the time to rupture associated with creep damage, compared with the smallest simple tube to quickly identify bayonet tube layouts that enhanced the receiver lifespan.

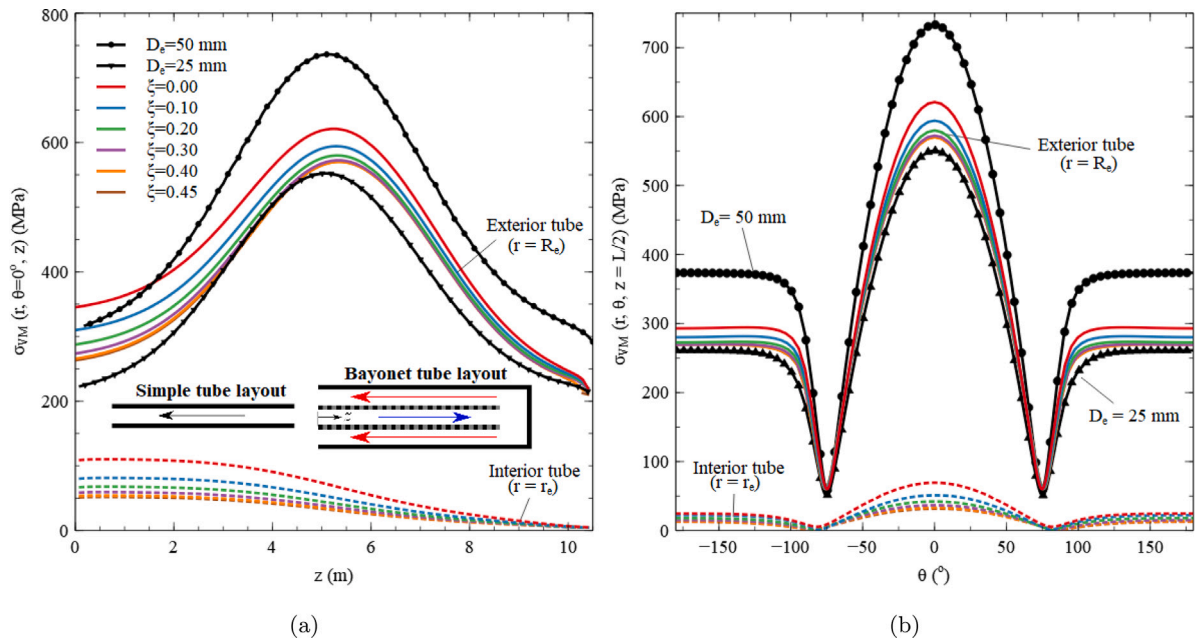


Fig. 12. For concentric ($\xi = 0$) and eccentric bayonet tubes ($\xi > 0$): (a) axial evolution of the maximum von Mises stress achieved for the tube, (b) circumferential distribution of the von Mises stress obtained at the outer tube surface. Solid lines: outer surface of the exterior tube of the bayonet tube. Dotted lines: outer surface of the interior tube of the bayonet tube. Solid black lines: outer surface of simple tubes.

Although the eccentric bayonet tube experiences a higher peak stress than the smallest simple tube, t_R is approximately 4.4% higher than the latter, demonstrating that bayonet tubes may be used as receiver tubes in SPT applications. In light of the results presented in this work, the bayonet tubes have great potential due to their capability to increase the convection heat transfer in the most thermally demanded zones. Nevertheless, their pressure drop is considerably higher than that obtained in conventional circular cross-section tubes. To compare both effects through a single parameter, the following overall thermal performance evaluation criterion (PEC) is proposed:

$$PEC = \frac{\bar{h}/\bar{h}_{ref}}{(\Delta P/\Delta P_{ref})^{1/3}} \quad (6)$$

Where ΔP is the total pressure drop of the HTF between the inlet and outlet of the tube and \bar{h} is the mean convection coefficient of heat transfer between the HTF and the tube wall heated by the concentrated sun radiation:

$$\bar{h} = \frac{\frac{1}{2\pi R_i L} \cdot \int_{z=0}^{z=L} \int_{\theta=-\pi}^{\theta=\pi} q''(r = R_i, \theta, z) R_i \cdot d\theta \cdot dz}{\frac{1}{2\pi R_i L} \cdot \int_{z=0}^{z=L} \int_{\theta=-\pi}^{\theta=\pi} T(r = R_i, \theta, z) R_i \cdot d\theta \cdot dz - \frac{1}{L} \cdot \int_{z=0}^{z=L} \bar{T}_{an}(z) dz} \quad (7)$$

In the above equation of PEC , the subindex ref denotes the reference case used to compare the performance of the tube. In this work, the reference case has been taken as the simple tube with either $D_e = 50$ mm or $D_e = 25$ mm, so that the influence of the reference tube diameter is shown in the PEC results. Note that, to take into account that the bayonet and the reference tubes have different configurations in the flow path, Eq. (6) directly compares \bar{h} and ΔP (the relevant parameters in this case) instead of the friction factor and Nusselt number commonly used in a PEC [72]. Table 4 shows the results of the PEC . The bayonet tube with eccentricity $\xi \geq 0.3$ improves the performance ($PEC > 1$) of conventional single tubes. This means that the increase of the convection coefficient in a bayonet tube can compensate for the increase in the pressure drop with regard simple tubes.

6. Conclusions

In this work, the thermomechanical performances of Haynes 230 bayonet tubes to be used as solar receivers were analyzed. A series of 3D CFD simulations were performed to characterize the effect of the eccentricity and the ratio of cross-sectional areas on the behavior of bayonet tubes under steady-state conditions. The solar noon of the spring equinox was selected as the representative day for the analysis. The same molten salt heat rate was used to perform a fair comparison between bayonet tube layouts. In the simulations of the present work, the eccentricity was varied from a concentric position, $\xi = 0.0$, until the walls of the exterior and interior tubes were almost touching, $\xi = 0.45$, to characterize their influence on the resulting thermal stresses in the tube walls of the bayonet receiver. The results revealed that the eccentricity created asymmetries in the flow characteristics that effectively increased the molten salt heat transfer coefficient on the outer tube where the annular section was wider; hence, in that region, the temperature and thermal stress were reduced. Furthermore, excessive overheating of the fluid was avoided since the heat absorbed by the outer tube was distributed between the flow of molten salt in the annular section and that in the circular section. As revealed by the simulations conducted, this effect was accentuated by the eccentricity between the centers of the inner and outer tubes of the bayonet tube.

Eccentric bayonet tube layouts caused the molten salt velocity to grow at the widest region of the annular section in eccentric configurations of the bayonet tube, producing the maximum flow velocities in this region, while the flow was considerably decelerated in the narrow region of the annular section. Eccentricity could reduce the pressure of the concentric bayonet tube configuration (3.61 bar) by 30.8%. Nevertheless, this pressure decrease was considerably higher than those obtained in the smallest and largest simple tubes, 1.28 bar and 0.13 bar, respectively. This enhancement of the tube wall cooling effect provoked by the eccentricity, which increased to 26.1% of the convective heat transfer achieved in a concentric configuration, was reflected in the maximum tube temperature, in which the peak temperature obtained in the concentric bayonet tube was diminished by approximately 4.9% with the highest eccentric configuration, which represented a temperature reduction of approximately 29.4 °C. In addition, this bayonet tube layout achieved a lower peak temperature than

Table 4

Maximum temperature and stress, pressure drop, time to rupture associated with creep damage and PEC for different receiver tubes layouts.

Type	D_e (mm)	ξ	T_{max} (°C)	$\sigma_{VM_{max}}$ (MPa)	$t_{creep}/t_{creep,D_e=25\text{ mm}}$ (-)	ΔP (bar)	\bar{h} (kW/m ² K)	PEC	
								$D_e = 50\text{ mm}$	$D_e = 25\text{ mm}$
Bayonet	50	0.00	593.5	618.2	0.14	3.61	10.57	0.65	0.68
		0.10	579.0	591.2	0.37	3.55	14.94	0.92	0.97
		0.20	570.5	575.7	0.66	3.44	15.84	0.98	1.04
		0.30	565.9	567.2	0.92	3.24	16.05	1.02	1.07
		0.40	564.1	563.7	1.04	3.01	16.44	1.07	1.12
		0.45	564.1	563.6	1.04	2.92	16.28	1.07	1.13
Simple	50	-	664.1	736.3	$3.23 \cdot 10^{-3}$	0.13	5.41	1.00	1.05
	25	-	569.4	552.1	1.28	1.28	10.99	0.95	1.00

simple tubes. The concentric bayonet tube achieved the highest thermal stress, i.e., 618.2 MPa, and it was reduced up to 8.8% as eccentricity increased. Although the smallest simple tube experienced a higher temperature than the eccentric bayonet tube, its lower inertial moment caused its maximum stress to be 2.1% lower than the stress obtained in the most eccentric layout analyzed in this work. Nevertheless, the time to rupture associated with creep damage of the eccentric bayonet tube was 4.4% higher than that obtained in the smallest simple tube. In addition, the tube's performance was evaluated through a *PEC* factor, which compared the mean convection heat transfer with the total pressure drop of the bayonet and the conventional tubes. The results indicate that the enhancement of convection achieved by the bayonet tube can compensate for the resulting increase of the pressure drop. The maximum *PEC* is obtained in the bayonet tube with high eccentricity ($\xi = 0.45$) and it is 7% and 13% higher than that obtained in a simple tube with $D_e = 50\text{ mm}$ and 25 mm , respectively. Based on the results presented in this work, it can be asserted that the bayonet tube could be a potential alternative to the current receiver tubes since it offers additional degrees of freedom, leading to an optimum in the thermomechanical behavior of the receiver.

Declaration of competing interest

The authors declare that they have no known competing financial interests or personal relationships that could have appeared to influence the work reported in this paper.

Data availability

No data was used for the research described in the article.

Acknowledgments

The authors gratefully acknowledge the financial support provided by the grants RTI2018-096664-B-C21 funded by FEDER/Ministerio de Ciencia e Innovación-Agencia Estatal de Investigación, Spain and PID2021-122895OB-I00 funded by MCIN/AEI/10.13039/501100011033 and by "ERDF A way of making Europe". This work was also financed by the Community of Madrid, Spain through the line of "Excelencia del Profesorado Universitario" of the Pluriannual Agreement with the UC3M, Spain (EPUC3M22), within the framework of the V PRICIT (V Plan Regional de Investigación Científica e Innovación Tecnológica). Rafael Pérez-Álvarez acknowledges support from the scholarship "Ayudas para contratos predoctorales para la formación de doctores" BES-2016-078455 awarded by the Ministerio de Economía, Industria y Competitividad, Spain.

References

- [1] M. Rodríguez-Sánchez, A. Soria-Verdugo, J.A.-I. nez, A. Acosta-Iborra, D. Santana, Thermal design guidelines of solar power towers, *Appl. Therm. Eng.* 63 (1) (2014) 428–438.
- [2] Y. Chen, Y. Zhang, D. Wang, X. Huang, Effects of design parameters on fatigue-creep damage of tubular supercritical carbon dioxide power tower receivers, *Renew. Energy* 176 (2021) 532–550.
- [3] B. Du, Y. He, Z. Zheng, Z. Cheng, Analysis of thermal stress and fatigue fracture for the solar tower molten salt receiver, *Appl. Therm. Eng.* 99 (2016) 741–750.
- [4] N. Boerema, G. Morrison, R. Taylor, G. Rosengarten, High temperature solar thermal central-receiver billboard design, *Sol. Energy* 97 (2013) 356–368.
- [5] M. Rodríguez-Sánchez, M. Laporte-Azcué, A. Montoya, F. Hernández-Jiménez, Non-conventional tube shapes for lifetime extend of solar external receivers, *Renew. Energy* 186 (2022) 535–546.
- [6] Y. Luo, X. Du, D. Wen, Novel design of central dual-receiver for solar power tower, *Appl. Therm. Eng.* 91 (2015) 1071–1081.
- [7] M. Qaisrani, J.W., J.F., Y.J., Z. Wan, M. Khalid, Heat losses and thermal stresses of an external cylindrical water/steam solar tower receiver, *Appl. Therm. Eng.* 163 (2019) 114241.
- [8] L. Yang, R. Zhou, X. Jin, X. Ling, H. Peng, Experimental investigate on thermal properties of a novel high temperature flat heat pipe receiver in solar power tower plant, *Appl. Therm. Eng.* 109 (2016) 610–618.
- [9] J. Pacio, C. Singer, T. Wetzel, R. Uhlig, Thermodynamic evaluation of liquid metals as heat transfer fluids in concentrated solar power plants, *Appl. Therm. Eng.* 60 (1) (2013) 295–302.
- [10] J. Pacio, T. Wetzel, Assessment of liquid metal technology status and research paths for their use as efficient heat transfer fluids in solar central receiver systems, *Sol. Energy* 93 (2013) 11–22.
- [11] W. Schiel, M. Geyer, Testing an external sodium receiver up to heat fluxes of 2.5 MW/m²: Results and conclusions from the IEA-SSPS high flux experiment conducted at the central receiver system of the Plataforma Solar de Almería (Spain), *Sol. Energy* 41 (3) (1988) 255–265.
- [12] C. Singer, R. Buck, R. Pitz-Paal, H. Müller-Steinhagen, Assessment of solar power tower driven ultrasupercritical steam cycles applying tubular central receivers with varied heat transfer media, *J. Sol. Energy Eng.* 132 (4) (2010).
- [13] R. Pérez-Álvarez, P. González-Gómez, A. Acosta-Iborra, D. Santana, Thermal stress and fatigue damage of central receiver tubes during their preheating, *Appl. Therm. Eng.* 195 (2021) 117115.
- [14] R. Pérez-Álvarez, P. González-Gómez, D. Santana, A. Acosta-Iborra, Preheating of solar power tower receiver tubes for a high-temperature chloride molten salt, *Appl. Therm. Eng.* (2022).
- [15] M. Fernández-Torrijos, C. Sobrino, C. Marugán-Cruz, D. Santana, Experimental and numerical study of the heat transfer process during the startup of molten salt tower receivers, *Appl. Therm. Eng.* 178 (2020) 115528.
- [16] M. Laporte-Azcué, P. González-Gómez, M.R. guez Sánchez, D. Santana, A procedure to predict solar receiver damage during transient conditions, *Renew. Sustain. Energy Rev.* 154 (2022) 111905.
- [17] M. Rodríguez-Sánchez, A. Sánchez-González, C. Marugán-Cruz, D. Santana, New designs of molten-salt tubular-receiver for solar power tower, *Energy Procedia* 49 (2014) 504–513, Proceedings of the SolarPACES 2013 International Conference.
- [18] R. Pérez-Álvarez, M. Rodríguez-Sánchez, A. Acosta-Iborra, D. Santana, Effect of eccentricity on the hydrodynamics and heat transfer of molten salt in bayonet receivers for solar power towers, *AIP Conf. Proc.* 2033 (1) (2018) 080004.
- [19] P. Wang, D. Liu, C. Xu, L. Zhou, L. Xia, Conjugate heat transfer modeling and asymmetric characteristic analysis of the heat collecting element for a parabolic trough collector, *Int. J. Therm. Sci.* 101 (2016) 68–84.
- [20] P. Wang, D. Liu, C. Xu, Numerical study of heat transfer enhancement in the receiver tube of direct steam generation with parabolic trough by inserting metal foams, *Appl. Energy* 102 (2013) 449–460, Special Issue on Advances in sustainable biofuel production and use - XIX International Symposium on Alcohol Fuels - ISAF.

- [21] C. Chang, A. Sciacovelli, Z. Wu, X. Li, Y. Li, M. Zhao, J. Deng, Z. Wang, Y. Ding, Enhanced heat transfer in a parabolic trough solar receiver by inserting rods and using molten salt as heat transfer fluid, *Appl. Energy* 220 (2018) 337–350.
- [22] R. Wolffe, Axial turbulent flow in a circular pipe containing a fixed eccentric core (Ph.D. thesis), Lehigh University (Bethlehem), 1962.
- [23] N. Dodge, Friction losses in annular flow, in: ASME Winter Annual Meeting, Paper, 1963.
- [24] W. Kays, E. Leung, Heat transfer in annular passages—hydrodynamically developed turbulent flow with arbitrarily prescribed heat flux, *Int. J. Heat Mass Transfer* 6 (7) (1963) 537–557.
- [25] V. Jonsson, E. Sparrow, Experiments on turbulent-flow phenomena in eccentric annular ducts, *J. Fluid Mech.* 25 (1) (1966) 65–86.
- [26] S. Kacker, Some aspects of fully developed turbulent flow in non-circular ducts, *J. Fluid Mech.* 57 (3) (1973) 583–602.
- [27] J. Nouri, H. Umur, J. Whitelaw, Flow of Newtonian and non-Newtonian fluids in concentric and eccentric annuli, *J. Fluid Mech.* 253 (1993) 617.
- [28] G. Choueiri, S. Tavoularis, Experimental investigation of flow development and gap vortex street in an eccentric annular channel. Part 1. Overview of the flow structure, *J. Fluid Mech.* 752 (2014) 521–542.
- [29] G. Choueiri, S. Tavoularis, Experimental investigation of flow development and gap vortex street in an eccentric annular channel. Part 2. Effects of inlet conditions, diameter ratio, eccentricity and Reynolds number, *J. Fluid Mech.* 768 (2015) 294–315.
- [30] D. Serrano, S. Sánchez-Delgado, R. Pérez-Álvarez, A. Acosta-Iborra, Experimental determination of the convection heat transfer coefficient in an eccentric annular duct, *Exp. Therm Fluid Sci.* 136 (2022) 110664.
- [31] R. Deissler, M. Taylor, Analysis of fully developed turbulent heat transfer and flow in an annulus with various eccentricities, 1955.
- [32] H. Usui, K. Tsuruta, Analysis of fully developed turbulent flow in an eccentric annulus, *J. Chem. Eng. Jpn.* 13 (6) (1980) 445–450.
- [33] H. Ninokata, T. Okumura, E. Merzari, T. Kano, Direct numerical simulation of turbulent flows in an eccentric annulus channel, *Annual Report of the Earth Simulator Center* April, 2006, 2005.
- [34] N. Nikitin, Direct numerical simulation of turbulent flows in eccentric pipes, *Comput. Math. Math. Phys.* 46 (3) (2006) 489–504.
- [35] N. Nikitin, H. Wang, S. Chernyshenko, Turbulent flow and heat transfer in eccentric annulus, *J. Fluid Mech.* 638 (2009) 95–116.
- [36] E. Merzari, H. Ninokata, Anisotropic turbulence and coherent structures in eccentric annular channels, *Flow Turbul. Combust.* 82 (1) (2009) 93–120.
- [37] R. Pérez-Álvarez, Optimization of Solar Thermal Plants: Transient Analysis and Design of Eccentric Bayonet Receivers (Ph.D. thesis), Thermal and fluid engineering department, Carlos III University, 2021.
- [38] M. Rodríguez-Sánchez, A. Sanchez-Gonzalez, C. Marugan-Cruz, D. Santana, Flow patterns of external solar receivers, *Sol. Energy* 122 (2015) 940–953.
- [39] M. Fahrman, S.K. Srivastava, Low cycle fatigue behaviour of HAYNES 230 alloy, *Mater. High Temp.* 31 (3) (2014) 221–225.
- [40] Haynes, Haynes 230 alloy: Principal Features (H-3000N). Haynes International, United States. , Technical Report, 2020, <https://www.haynesintl.com/>.
- [41] A. Zavoico, Solar power tower design basis document, revision 0, Technical Report, Sandia National Labs, 2001.
- [42] W.S. Slemp, W.R. Wade, A method for measuring the spectral normal emittance in air of a variety of materials having stable emittance characteristics, *Measurement of Thermal Radiation Properties of Solids*, NASA SP-31 (1963) 433–439.
- [43] P.K. Falcone, A handbook for solar central receiver design, Technical Report, 1986.
- [44] J. Lata, S. Alcalde, D. Fernández, X. Lekube, First surrounding field of heliostats in the world for commercial solar power plants-gemasolar, in: 16th International SolarPACES Symposium, 2010.
- [45] H. Zhang, Z. Wang, M. Guo, W. Liang, Cosine efficiency distribution of heliostats field of solar thermal power tower plants, in: 2009 Asia-Pacific Power and Energy Engineering Conference, 2009, pp. 1–4.
- [46] A. Sánchez-González, M. Rodríguez-Sánchez, D. Santana, Aiming factor to flatten the flux distribution on cylindrical receivers, *Energy* 153 (2018) 113–125.
- [47] ANSYS, ANSYS 19 fluent user guide, *Comput. Methods Appl. Mech. Engrg.* (2019).
- [48] F. Menter, Two-equation eddy-viscosity turbulence models for engineering applications, *AIAA J.* 32 (8) (1994) 1598–1605.
- [49] S. Acharya, B. Baliga, K. Karki, J. Murthy, C. Prakash, S. Vanka, Pressure-based finite-volume methods in computational fluid dynamics, 2007.
- [50] S. Patankar, D. Spalding, A calculation procedure for heat, mass and momentum transfer in three-dimensional parabolic flows, *Int. J. Heat Mass Transfer* 15 (10) (1972) 1787–1806.
- [51] T. Barth, D. Jespersen, The design and application of upwind schemes on unstructured meshes, in: 27th Aerospace Sciences Meeting, 1989.
- [52] Z. Ying, B. He, L. Su, Y. Kuang, D. He, C. Lin, Convective heat transfer of molten salt-based nanofluid in a receiver tube with non-uniform heat flux, *Appl. Therm. Eng.* 181 (2020) 115922.
- [53] V. Gnielinski, New equations for heat and mass transfer in turbulent pipe and channel flow, *NASA STI/Recon Technical Report A 41* (1) (1975) 8–16.
- [54] C. Monrad, J. Pelton, Heat transfer by convection in annular spaces, *Trans. AIChE* 38 (1942) 593–611.
- [55] M. Laporte-Azcué, P. González-Gómez, M. Rodríguez-Sánchez, D. Santana, Deflection and stresses in solar central receivers, *Sol. Energy* 195 (2020) 355–368.
- [56] W. Logie, J. Pye, J. Coventry, Thermoelastic stress in concentrating solar receiver tubes: A retrospect on stress analysis methodology, and comparison of salt and sodium, *Sol. Energy* 160 (2018) 368–379.
- [57] J. Jones, Effects of bending on the fatigue life of solar receiver tubes subjected to one-sided heating, 1979.
- [58] S. Pai, On turbulent flow in circular pipe, *J. Franklin Inst. B* 256 (4) (1953) 337–352.
- [59] D. Taler, Determining velocity and friction factor for turbulent flow in smooth tubes, *Int. J. Therm. Sci.* 105 (2016) 109–122.
- [60] W. Lloyd, G. Hedrick, Preparation and beckmann rearrangement of pinonic acid oxime, *Ind. Eng. Chem. Prod. Res. Dev.* 2 (2) (1963) 143–145.
- [61] D. Bhandari, S. Singh, Analysis of fully developed turbulent flow in a pipe using computational fluid dynamics, *Int. J. Eng. Res. Technol.* 1 (2012).
- [62] E. Canlı, A. Ates, S. Bilir, Developing turbulent flow in pipes and analysis of entrance region, *Academic Platform - J. Eng. Sci.* (2021) 332–353.
- [63] P. Bradshaw, Turbulent secondary flows, *Annu. Rev. Fluid Mech.* 19 (1) (1987) 53–74.
- [64] R. Pérez-Álvarez, M. Rodríguez-Sánchez, A. Acosta-Iborra, D. Santana, Effect of eccentricity on the hydrodynamics and heat transfer of molten salt in bayonet receivers for solar power towers, 2033, 2018, 080004.
- [65] C. Marugán-Cruz, O. Flores, D. Santana, M. Garci a Villalba, Heat transfer and thermal stresses in a circular tube with a non-uniform heat flux, *Int. J. Heat Mass Transfer* 96 (2016) 256–266.
- [66] R. Pérez-Álvarez, M. Laporte-Azcué, A. Acosta-Iborra, D. Santana, Effect of eccentricity on the thermal stresses in a bayonet tube for solar power tower receivers, *AIP Conf. Proc.* 2126 (2019) 030041.
- [67] R. Pérez-Álvarez, C. Marugan-Cruz, D. Santana, A. Acosta-Iborra, Comparison of the heat transfer characteristics of molten salt, liquid sodium and supercritical CO₂ in bayonet tubes of solar tower receivers, *AIP Conf. Proc.* 2126 (2019) 080005.
- [68] F. Dittus, L. Boelter, Heat transfer in automobile radiators of the tubular type, *Int. Commun. Heat Mass Transfer* 12 (1) (1985) 3–22.
- [69] H. Zhou, Y. Li, Y. Zuo, M. Zhou, W. Fang, Y. Zhu, Thermal performance and thermal stress analysis of a 600 MWth solar cylinder external receiver, *Renew. Energy* 164 (2021) 331–345.
- [70] P. González-Gómez, M. Rodríguez-Sánchez, M. Laporte-Azcué, D. Santana, Calculating molten-salt central-receiver lifetime under creep-fatigue damage, *Sol. Energy* 213 (2021) 180–197.
- [71] D. Eno, G. Young, T. Sham, A unified view of engineering creep parameters, in: ASME Pressure Vessels and Piping Conference, 48296, 2009, pp. 777–792.
- [72] R. Webb, Performance evaluation criteria for use of enhanced heat transfer surfaces in heat exchanger design, *Int. J. Heat Mass Transfer* 24 (4) (1981) 715–726.